Shallow Calcium Carbonate Cycling in the North Pacific Ocean

Adam Subhas, Sijia Dong, John Naviaux, Nick Rollins, Patrizia Ziveri, William Gray, James Rae, Xuewu Liu, Robert Byrne, Sang Chen, et al.

HAL Id: hal-03682866

https://hal.science/hal-03682866

Submitted on 31 May 2022

Shallow Calcium Carbonate Cycling in the North Pacific Ocean

Adam V. Subhas[1] , Sijia Dong[2] , John D. Naviaux[3], Nick E. Rollins[4], Patrizia Ziveri[5,6], William Gray[7] , James W. B. Rae[8] , Xuewu Liu[9], Robert H. Byrne[9], Sang Chen[10] , Christopher Moore[9] , Loraine Martell-Bonet[9] , Zvi Steiner[11] , Gilad Antler[12], Huanting Hu[10], Abby Lunstrum[4], Yi Hou[13] , Nathaniel Kemnitz[4], Johnny Stutsman[14], Sven Pallacks[5], Mathilde Dugenne[15], Paul D. Quay[14] , and William M. Berelson[4], and Jess F. Adkins[2]

[1]Department of Marine Chemistry and Geochemistry, Woods Hole Oceanographic Institution, Woods Hole, MA, USA, [2]Division of Geological and Planetary Sciences, California Institute of Technology, Pasadena, CA, USA, [3]Four Twenty Seven Inc., Sunnyvale, CA, USA, [4]Department of Earth Sciences, University of Southern California, Los Angeles, CA, USA, [5]Institut de Ciencia I Tecnologia Ambientals, Universitat Autonoma de Barcelona, Barcelona, Spain, [6]Catalan Institution for Research and Advanced Studies (ICREA), Barcelona, Spain, [7]Laboratorie des Sciences du Climat et de l'Environnement (LSCE/IPSL), Universite Paris-Saclay, Gif-sur-Yvette, France, [8]School of Earth and Environmental Sciences, University of St Andrews, St Andrews, Scotland, [9]College of Marine Science, University of South Florida, St. Petersburg, FL, USA, [10]School of Oceanography, Shanghai Jiao Tong University, Shanghai, China, [11]GEOMAR, Helmholtz Centre for Ocean Research Kiel, Kiel, Germany, [12]Department of Earth and Environmental Sciences, Ben-Gurion University, Be'er Sheva, Israel, [13]Department of Earth, Environmental, and Planetary Sciences, Rice University, Houston, TX, USA, [14]School of Oceanography, University of Washington, Seattle, WA, USA, [15]School of Ocean and Earth Science and Technology, University of Hawaii, Honolulu, HI, USA

Abstract The cycling of biologically produced calcium carbonate ($CaCO_3$) in the ocean is a fundamental component of the global carbon cycle. Here, we present experimental determinations of in situ coccolith and foraminiferal calcite dissolution rates. We combine these rates with solid phase fluxes, dissolved tracers, and historical data to constrain the alkalinity cycle in the shallow North Pacific Ocean. The in situ dissolution rates of coccolithophores demonstrate a nonlinear dependence on saturation state. Dissolution rates of all three major calcifying groups (coccoliths, foraminifera, and aragonitic pteropods) are too slow to explain the patterns of both $CaCO_3$ sinking flux and alkalinity regeneration in the North Pacific. Using a combination of dissolved and solid-phase tracers, we document a significant dissolution signal in seawater supersaturated for calcite. Driving $CaCO_3$ dissolution with a combination of ambient saturation state and oxygen consumption simultaneously explains solid-phase $CaCO_3$ flux profiles and patterns of alkalinity regeneration across the entire N. Pacific basin. We do not need to invoke the presence of carbonate phases with higher solubilities. Instead, biomineralization and metabolic processes intimately associate the acid (CO_2) and the base ($CaCO_3$) in the same particles, driving the coupled shallow remineralization of organic carbon and $CaCO_3$. The linkage of these processes likely occurs through a combination of dissolution due to zooplankton grazing and microbial aerobic respiration within degrading particle aggregates. The coupling of these cycles acts as a major filter on the export of both organic and inorganic carbon to the deep ocean.

Plain Language Summary The marine carbon cycle is made of organic carbon and calcium carbonate ($CaCO_3$) components. While the organic carbon cycle has received much attention, the $CaCO_3$ cycle is relatively understudied. Through a dedicated research expedition to the North Pacific Ocean, we demonstrate here a coupling of these two cycles, stemming from the fact that all organisms that produce $CaCO_3$ also produce intimately associated organic carbon. We suggest that the mechanisms responsible for the formation and sinking of organic carbon particles in the ocean are likely as important for $CaCO_3$ export, and that the respiration of organic carbon is responsible for the dissolution of a substantial portion of $CaCO_3$ in the upper ocean.

1. Introduction

The marine calcium carbonate ($CaCO_3$) cycle is integral to the global carbon cycle. The production of biogenic $CaCO_3$ tends to raise atmospheric CO_2 due to consumption of surface ocean alkalinity, while the ballasting of organic matter and export into the deep ocean provided by this material tends to lower CO_2 (De La Rocha

Martell-Bonet, Zvi Steiner, Gilad Antler, Huanting Hu, Abby Lunstrum, Yi Hou, Nathaniel Kemnitz, Johnny Stutsman, Sven Pallacks, Mathilde Dugenne, Paul D. Quay, William M. Berelson
Methodology: Adam V. Subhas, John D. Naviaux, Nick E. Rollins, Patrizia Ziveri, Xuewu Liu, Robert H. Byrne, William M. Berelson, Jess F. Adkins
Project Administration: Adam V. Subhas, William M. Berelson, Jess F. Adkins
Resources: Robert H. Byrne, William M. Berelson
Supervision: William M. Berelson
Validation: Patrizia Ziveri
Visualization: Adam V. Subhas
Writing – original draft: Adam V. Subhas
Writing – review & editing: Adam V. Subhas, Sijia Dong, John D. Naviaux, Patrizia Ziveri, William Gray, James W. B. Rae, Robert H. Byrne, Zvi Steiner, Gilad Antler, Abby Lunstrum, Nathaniel Kemnitz, Sven Pallacks, Mathilde Dugenne, William M. Berelson, Jess F. Adkins

et al., 2008; Klaas & Archer, 2002; Passow & De La Rocha, 2006). In addition to these roles, solid $CaCO_3$ is crucial to the neutralization of CO_2 through its dissolution and associated production of ocean alkalinity (Archer et al., 1998). Despite consensus on the general dynamics of marine $CaCO_3$ cycling, rates of $CaCO_3$ production and dissolution are poorly constrained (Battaglia et al., 2016; Berelson et al., 2007; Dunne et al., 2012). If a substantial amount of alkalinity is regenerated in the shallow ocean where precipitation is thermodynamically favored, then the traditional relationship between water column $CaCO_3$ dissolution rates and mineral saturation state must be reexamined.

The formation and dissolution of calcium carbonate minerals is canonically described as a function of seawater saturation state $\left(\Omega = \left[Ca^{2+} \right] \left[CO_3^{2-} \right] / K'_{sp} \right)$, where K'_{sp} is the in situ apparent solubility product of the $CaCO_3$ mineral of interest (e.g., calcite or aragonite). The dissolution rate R is empirically related to Ω using the equation $R = k(1-\Omega)^n$, where k is the specific dissolution rate constant, and n is a fit parameter describing the nonlinearity of dissolution rate as a function of undersaturation (Keir, 1980). In brief, calcite dissolution is a highly nonlinear function of seawater undersaturation across a wide range of saturation states, an observation that dates back to early experiments by Peterson (1966) and Berner and Morse (1974).

This high degree of nonlinearity can be explained by applying kinetic crystal growth models to calcite dissolution, as summarized in Adkins et al. (2021) for inorganic calcite. As saturation state decreases, inorganic calcite dissolution goes through distinct rate transitions at "critical" Omega values (Ω_{crit}, Dong, Berelson, Adkins, et al., 2020; Naviaux, Subhas, Rollins, et al., 2019). At colder temperatures, a single break in slope in log(rate) versus log(1−Ω) is observed at an Ω_{crit} ~0.75–0.8, marking the transition between dissolution at step-edges and dissolution on the 2D mineral surface (Figure 1 black envelope, Dong et al., 2019; Naviaux, Subhas, Dong, et al., 2019; Naviaux, Subhas, Rollins, et al., 2019; Peterson, 1966). Practically, two dissolution regimes mean that calcite dissolution in seawater is best described by two rate equations, uniquely defined between $1 > \Omega > \Omega_{crit}$ and $\Omega_{crit} > \Omega > 0$, each with distinct $k−n$ pairs. Near equilibrium, dissolution rate is slow and relatively insensitive to saturation state with a small k and $n < 1$. Far from equilibrium, dissolution rapidly increases as a function of undersaturation, leading to a large k and $n >> 1$. Several in situ water column dissolution experiments with inorganic calcite have documented this sharp increase in dissolution rate below Ω_{crit} (Honjo & Erez, 1978; Naviaux, Subhas, Dong, et al., 2019; Peterson, 1966).

Like inorganic calcite, biogenic calcites and aragonite demonstrate a rate transition at the same Ω_{crit} as inorganic calcite (Dong et al., 2019; Subhas et al., 2018). Biogenic calcite dissolution rates demonstrate k and n values that are distinct from the inorganic calcite curve (Figure 1, red envelope). Coccolith dissolution rates appear to behave similarly to calcite near equilibrium, but are less sensitive to saturation state far-from-equilibrium ($n = 2.2$, Subhas et al., 2018). Foraminifera also demonstrate a far-from-equilibrium $n \sim 2$. They appear to dissolve faster than coccoliths normalized by both mass and by surface area, suggesting that foraminifera require their own specific k values (Gehlen et al., 2005; Subhas et al., 2018; Subhas, McCorkle, et al., 2019). Aragonite dissolves more slowly than biogenic calcite, and also has the lowest $n \sim 1.8$ (Dong et al., 2019). Compared to inorganic calcite, the lower sensitivity of biogenic calcite dissolution to saturation state, particularly farther from equilibrium, is potentially due to the presence of organic templates and matrices within the calcite structure (e.g., Subhas et al., 2018; Walker & Langer, 2021). Differences in specific k and n values aside, it appears that all calcium carbonates dissolve slowly near equilibrium, and only rapidly increase their dissolution rates once Ω drops below $\Omega_{crit} \sim 0.8$ for the colder temperatures of the modern water column.

Contrary to these experiments, most oceanographic observations of $CaCO_3$ dissolution argue for a large dissolution flux in the shallow ocean, where waters are typically supersaturated, followed by relatively little dissolution in the deep ocean, where waters are more deeply undersaturated. The mechanisms driving this large shallow dissolution flux are confusing, because they cannot be explained by rate relationships between saturation state and dissolution rate. This conundrum was posed explicitly by Milliman et al. (1999), who postulated that balancing global $CaCO_3$ production and burial required a large shallow dissolution flux. This shallow dissolution flux was then matched to the appearance of excess alkalinity in the Pacific (Feely et al., 2002) and Atlantic basins (Chung et al., 2003). Later, some researchers argued that the appearance of excess alkalinity above the calcite saturation horizon is complicated by water mass transport and mixing processes (Battaglia et al., 2016; Carter et al., 2021; Friis et al., 2006). Recent modeling efforts have shown that a supersaturated alkalinity signal is due to a combination of circulation and dissolution, lending support to the presence of a shallow $CaCO_3$ cycle (Carter et al., 2021; Sulpis et al., 2021).
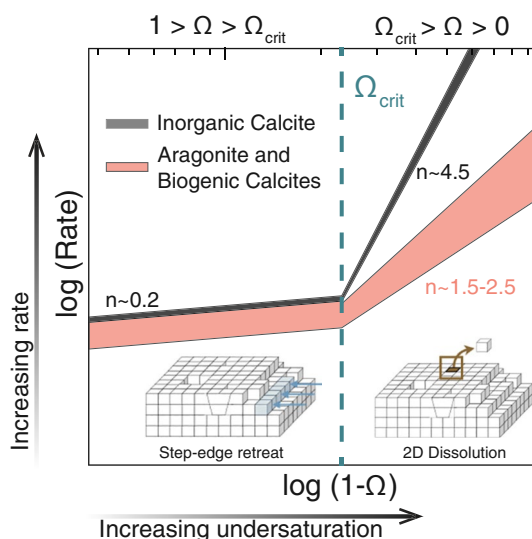
Figure 1. A schematic of surface area-normalized log(rate) as a function of $\log(1-\Omega)$ at 5°C, for inorganic calcite (black) and aragonite and biogenic calcites (red), adapted from Naviaux, Subhas, Dong, et al. (2019), Naviaux, Subhas, Rollins, et al. (2019), Subhas et al. (2018), and Dong et al. (2019). The dashed line denotes Ω_{crit}, the value of Ω at which the dissolution mechanism shifts from near-equilibrium step-edge retreat to far-from-equilibrium 2-dimensional, homogenous dissolution. All biogenic calcites, and aragonite, demonstrate a rate transition at the same Ω_{crit} as inorganic calcite, but demonstrate a shallower far-from-equilibrium slope compared to inorganic calcite. The larger red envelope is intended to illustrate the larger range in dissolution rates of biogenic materials. Logarithmically spaced ticks for $1-\Omega$ are shown at the top of the plot for clarity.

Numerous observations of particulate $CaCO_3$ loss in the upper water column serve as a complement to the appearance of dissolved alkalinity (Barrett et al., 2014; Bishop & Wood, 2008; Bishop et al., 1980, 1986; Dong et al., 2019; Milliman et al., 1999; Timothy et al., 2013; Troy et al., 1997; Wong et al., 1999). Some authors have attempted to explain these observations through the production and dissolution of more soluble $CaCO_3$ polymorphs such as aragonite (Buitenhuis et al., 2019; Feely et al., 2002), and pelagic fish-produced Mg-calcite, and amorphous carbonates (S. E. Wilson et al., 2008; Woosley et al., 2012). The total production of these "missing" highly soluble phases remains poorly constrained, and therefore their contribution to the shallow $CaCO_3$ cycle remains an open question.

An alternate hypothesis is that the aggregation of marine snow and the grazing activity of zooplankton create hotspots of calcium carbonate dissolution (Bishop et al., 1980; Milliman et al., 1999). The interiors of marine snow aggregates and zooplankton guts both exhibit lower pH, and therefore lower Ω, than ambient seawater, due to the production of respiratory CO_2 and digestive acids (Alldredge & Cohen, 1987; Pond et al., 1995). These grazing and aggregation processes are recognized as fundamental to total carbon export from the euphotic zone through the mesopelagic (Boyd et al., 2019; Grabowski et al., 2019; Henson et al., 2019), and they would allow more abundant phases like coccolith and foraminiferal calcite to play a role in shallow water column dissolution.

Here, we present new results and analyses from the CDisK-IV research expedition, occupying five stations in the North Pacific from Hawaii to Alaska in the summer of 2017. We present new in situ dissolution rate measurements of coccolith and foraminiferal calcite using a ^{13}C-tracer approach (Naviaux, Subhas, Dong, et al., 2019; Subhas et al., 2015). The quantification of in situ dissolution rates across a wide range of saturation states allows us to estimate the magnitude of ambient Ω-driven water column $CaCO_3$ dissolution, with explicit contributions from the three main calcifier groups (coccoliths, foraminifera, and pteropods) to the total $CaCO_3$ dissolution flux. In order to assess the significance of dissolution above the saturation horizon, we present new analyses of dissolved water column carbonate chemistry and oxygen data that complement the canonical excess alkalinity approach. Finally, we attempt to reconcile these in situ dissolution rate measurements and our own analyses with historical observations of a large, shallow dissolution cycle in the North Pacific Ocean.

2. Materials and Methods

2.1. Study Area

The North Pacific is a key region for constraining $CaCO_3$ cycling, due to the large portion of the water column that is undersaturated for calcite and aragonite (Figure 2a), and the foundational studies on changes in saturation horizon and degree of carbonate dissolution performed there (Feely et al., 2002; Friis et al., 2006; Peterson, 1966; Sabine et al., 2004). We conducted the CDisK-IV cruise on the R/V Kilo Moana in the North Pacific Ocean during August 2017, on a transect from Honolulu, HI to Seward, AK. At five survey stations (Figure 2 gray points, Table 1) we measured an extensive range in saturation states (Ω, defined as $[Ca^{2+}][CO_3^{2-}]/K'_{sp}$, where K'_{sp} is the apparent solubility of the carbonate mineral; Figure 2a), and established a spatial gradient in $CaCO_3$ production ecology. Quantitative $CaCO_3$ mineralogy, ecology, standing stock, production, and export flux measurements along this transect are presented elsewhere (Dong et al., 2019; Ziveri et al., 2022). We complemented these solid-phase measurements by sampling the full water column for its dissolved inorganic carbon (DIC), total alkalinity (Alk), pH, and $\delta^{13}C$ of DIC; and deployed custom-built in situ incubators to measure biogenic calcite dissolution rates as a function of water column chemistry. The dissolution rates of aragonite and inorganic calcite are presented in detail elsewhere (Dong et al., 2019; Naviaux, Subhas, Dong, et al., 2019).
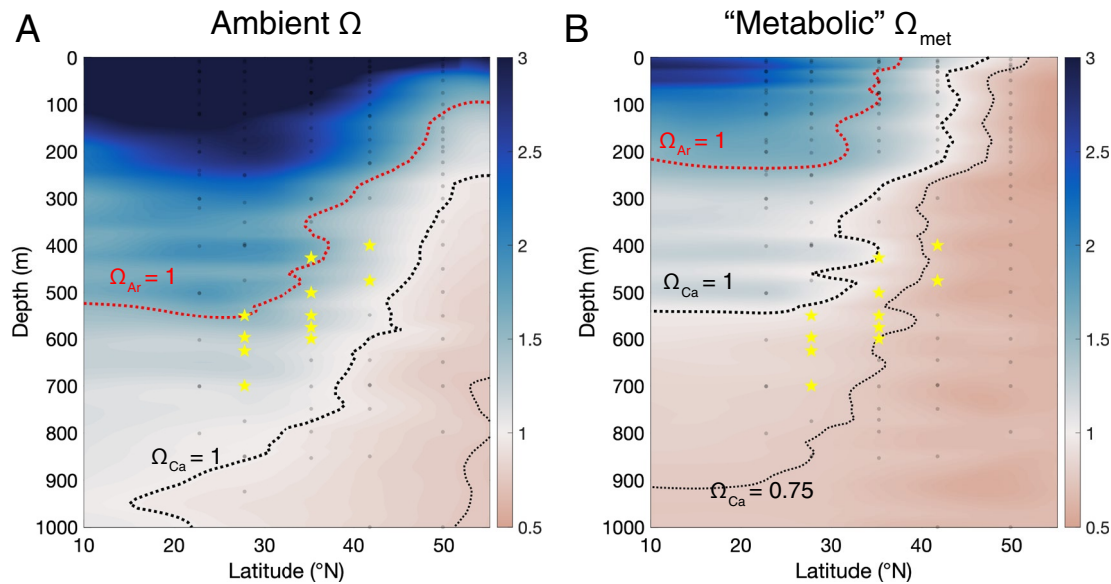
Figure 2. Carbonate chemistry of the upper 1,000 m of the North Pacific Ocean. (a) Depth-latitude zonal section of in situ Ω calculated using Alk and dissolved inorganic carbon data from the GLODAPv2.2019 database. Color bar indicates $\Omega_{calcite}$. Red and black dashed lines denote the aragonite and calcite saturation horizons (defined as $\Omega = 1$), respectively. Gray points indicate sampling locations during our 2017 research expedition (Table 1). Yellow stars indicate the location of North Pacific Intermediate Water (main text for details). (b) A calculation of Ω_{met} for calcite along the section in (a). The 0.75 calcite "isosat" is shown to demonstrate the potential for deep undersaturation within confined environments in the upper water column.

2.2. Sediment Traps

Sediment trap protocols can be found in companion papers by Subhas, Adkins, et al. (2019) and Dong et al. (2019) and are outlined briefly here. Two sediment traps positioned at 100 and 200 m on a single line were deployed at each station as a floating array. Each trap consisted of 12 polycarbonate particle interceptor tubes (70 cm long, 10 cm diameter) mounted on a circular frame, with a baffle grid to screen for macrofauna (Haskell et al., 2016, Figure S1 in Supporting Information S1 for picture). Sinking material was funneled into a 50 mL falcon tube at the base of each tube. Falcon tubes were filled with 30 mL of buffer solution, prepared following US JGOFS protocol. Six random tubes were combined, and "swimmers" (mostly large copepods, amphipods and larvae) were picked out. The samples were filtered onto a pre-weighed glass fiber filter (Whatman glass GF/F, 1825-047), which was then used to calculate mass flux and mineralogy via X-ray diffraction. Particulate inorganic carbon (PIC) and total carbon fluxes were calculated using established methods (Dong et al., 2019).

Table 1
Station Locations and Flux Data for the CDisK-IV Cruise

Station	Latitude	Longitude	Date occupied	$F_{PIC,100 m}$	$F_{PIC,200 m}$	f_{arag}	f_{cocco}
1[a]	22 45′	157 59′	2–4 August 2017	0.71	N.A.	0.44	0.98
2	27 45′	155 15′	6–10 August 2017	0.50	0.32	0.75	0.99
3	35 16′	150 59′	12–15 August 2017	0.13	N.A.	0.50	1.00
4	41 45′	148 16′	16–19 August 2017	2.23	0.82	0.10	0.83
5[b]	49 50′	149 39′	21–26 August 2017	1.03	0.75	0.09	0.90

Note. Floating sediment trap PIC fluxes (F) are in units of mmol m^{-2} d^{-1}, subscript is trap depth. PIC fluxes, and the fraction of total calcium carbonate as aragonite (f_{arag}), are from Dong et al. (2019). The fraction of calcite is calculated as $1 - f_{arag}$. The mixed layer calcite inventory is further split into coccolith and foraminiferal fractions, with f_{cocco} representing the coccolith calcite fraction (Ziveri et al., 2022).
[a]Station 1 was located at Station ALOHA (22 45′N, 158′W). [b]Station 5 was located near Ocean Station Papa (OSP; 50 06′N, 144 54′W).

2.3. Dissolved Carbonate System and Nutrient Measurements

Methods for total alkalinity, pH, $\delta^{13}C_{DIC}$, silica, and nutrient measurements are well established, and have been reported previously (Dong et al., 2019; Naviaux, Subhas, Dong, et al., 2019). DIC and secondary measurements of $\delta^{13}C$ were measured on Niskin rosette samples using a custom Picarro-based system developed at the University of South Florida (USF) and at University of Southern California (USC). Samples were collected in 300 ml biological oxygen demand (BOD) bottles in a manner similar to that used for alkalinity samples, with the exception that the bottle had a 5 ml headspace and was poisoned using a saturated $HgCl_2$ solution. The DIC instrument was housed in a 15 gallon insulated cooler that was capable of accommodating 10 samples including a certified reference material (CRM). After a brief tubing rinse, the sample was pumped from the BOD bottle to a 20 ml glass bulb that was submerged in a thermostatted water bath. An acid pump injected 3 ml of 17% H_3PO_4 into the top of the glass bulb. A three-way valve was then switched, allowing carrier gas to push the acidified sample into the purging tube, and the CO_2 gas evolved was measured on a Picarro 2131-i instrument. The software first recorded a baseline reading while N_2 was flowing in the system, and a threshold signal of 70 ppm triggered the peak detection. Once a signal was detected, the peak integration continued until the signal returned to the baseline. The DIC purging time was set to be longer than the required integration time to ensure all CO_2 was detected. Total counts of both ^{12}C and ^{13}C were obtained. The $^{13}C/^{12}C$ ratio was calculated based on total peak integrations. Since ratios are based on total ^{12}C and ^{13}C, potential fractionation of carbon during purging is avoided. Sample $^{13}C/^{12}C$ ratios and total DIC concentrations were linked to measured CRM solutions, and agree within error to Niskin $\delta^{13}C$ values measured by the CalTech/USC group (Naviaux, Subhas, Dong, et al., 2019). We use the Caltech/USC $\delta^{13}C$ and USF DIC values here.

2.4. Biogenic CaCO₃ Dissolution Experiments

Dissolution experiments were conducted in situ using modified Niskin incubators, described in detail by Naviaux, Subhas, Dong, et al. (2019) and Dong et al. (2019). In this study, we report dissolution rates of bleached, ^{13}C-labeled *E. huxleyi* liths. A total of 20 coccolith dissolution experiments were conducted at depths between 240 and 1,000 m at Stations 2–5 with temperatures ranging from 2.4 to 4.8°C and $\Omega_{calcite}$ from 0.96 to 0.67. We conducted one experiment with a planktic foraminiferal assemblage, cultured and ^{13}C-labeled as described in Subhas et al. (2018). Roughly 0.5–1.5 mg of labeled biogenic calcite was sealed in between 47 mm diameter "Nuclepore" polycarbonate membrane filters (0.8 μm pore size). This preparation has no effect on net dissolution rates, as documented by Naviaux, Subhas, Dong, et al. (2019). These packets were then mounted inside the Niskin incubators. The incubators were hung on a hydrowire, sent down to depth, and triggered closed. As a closed system, a pump continuously circulated water from the housing holding the packets into the Niskin. The Niskin reactors remained closed at depth for 24–58 hr and were sampled for silica, soluble reactive phosphorus (SRP), nitrate, alkalinity, pH, and $\delta^{13}C$-DIC upon recovery. Niskin data were quality checked by comparing SRP, silica, and nitrate to ambient water-column values obtained via CTD/rosette deployments on the same cruise. Saturation states in the Niskin reactors were determined from Alk-pH pairs, input into CO2SYS along with the temperature, salinity, depth, SRP, and silica concentrations at which the reactor was deployed. Dissolution rates were calculated by taking the difference between the final incubator and ambient water column $^{13}C/^{12}C$ ratios, multiplied by the [DIC] and the mass of seawater (1.126 kg) inside the incubators, and divided by the incubation time (Naviaux, Subhas, Dong, et al., 2019). Biogenic materials were not 100% labeled and rates were scaled for the extent of isotope labeling following Subhas et al. (2018). Briefly, when the amount of ^{13}C in the dissolving material is greatly enriched above natural abundance ($^{13}C/^{12}C \sim 0.01$), isotope ratio differences can be multiplied by a correction factor of $(R_s + 1)/R_s$, where R_s is the $^{13}C/^{12}C$ ratio of the dissolving solid (i.e., a reduced form of Equation 3 from Subhas et al., 2018). One batch of ^{13}C-labeled *E. huxleyi* was used for all dissolution rates shown here ($R_s = 0.928$), except for one experiment that used an older batch ($R_s = 20$, Subhas et al., 2018). The planktic foraminifera assemblage from Subhas et al. (2018) was used ($R_s = 1.6$). Adjusting the rates using these R_s values gives mass-normalized rates in units of g CaCO₃ g⁻¹ d⁻¹. Mass-normalized dissolution rates were further divided by the specific surface areas of *E. huxlyei* liths (105,000 cm² g⁻¹) and planktic foraminifera (43,000 cm² g⁻¹, Subhas et al., 2018) and the molar mass of calcium carbonate (100 g mol⁻¹) to generate specific dissolution rates for each calcite type in units of mol CaCO₃ cm⁻² d⁻¹.

Table 2
Regression Parameters for the Rate Equation Rate = k(1−Ω)ⁿ for the Dissolution Rate Data Shown in Figure 3, and Used in the Dissolution Rate Model (Section 2.4)

	$1 > \Omega > 0.78$			$0.78 > \Omega > 0$		
	$\log_{10}k_{mass}$ g g^{-1}d^{-1}	$\log_{10}k_{sa}$ mol cm^{-2}s^{-1}	n	$\log_{10}k_{mass}$ g g^{-1}d^{-1}	$\log^{10}k_{sa}$ mol cm^{-2}s^{-1}	n
E. hux lab 21°C[a]	−1.8 ± 0.1	−13.7 ± 0.1	0.33 ± 0.09	−0.31 ± 0.1	−12.4 ± 0.1	2.2 ± 0.1
E. hux in situ	−2.5 ± 0.1	−14.5 ± 0.1	0.18 ± 0.16	−1.3 ± 0.3	−13.3 ± 0.3	2.1 ± 0.5
Foram assemblage lab 21°C[a]	−	−	−	−0.35 ± 0.05	−11.9 ± 0.2	1.7 ± 0.1
E. hux in situ × 1.6	−2.32 ± 0.14	−14.28 ± 0.14	0.18 ± 0.16	−1.1 ± 0.3	−12.8 ± 0.3	2.1 ± 0.5
Aragonite in situ[b]	−2.74 ± 0.19	−14.02 ± 0.19	0.24 ± 0.19	−1.75 ± 0.15	−13.03 ± 0.15	1.76 ± 0.36

Note. We report k_{mass} (dissolution rate constant normalized to mass), k_{sa} (k_{mass} further normalized to specific surface area) and n (reaction exponent) for the regions near equilibrium above Ω_{crit} (=0.78), and far from equilibrium below Ω_{crit}. To estimate foraminiferal dissolution rates, the in situ mass-normalized *E. hux* data was multiplied by a factor of 1.6 (see text for details).
[a]Laboratory data are from Subhas et al. (2018). [b]Aragonite field data are from Dong et al. (2019).

2.5. 1-D CaCO₃ Flux and Dissolution Calculations

We constructed a one-dimensional model of particulate CaCO₃ sinking and dissolution, combining our measurements of CaCO₃ export fluxes and export mineralogy (Table 1); ambient seawater Ω; and aragonite, foraminiferal, and coccolith dissolution kinetics (Table 2). This model extends the analysis of Dong et al. (2019) to coccolith, foraminifera, and aragonite dissolution at all five survey stations. The model was initiated with our measured 100 m sinking PIC fluxes, partitioned into aragonite and calcite:

$$F_{arag} = F_{tot}f_{arag};$$

$$F_{calc} = F_{tot}\left(1 - f_{arag}\right),$$

where F_{tot} is the total PIC export flux at 100 m, and f_{arag} is the fraction of total CaCO₃ as aragonite measured in the sinking flux (Table 1, Dong et al., 2019). The dissolution flux for each phase was then calculated at all depths for which we acquired water column dissolution data (at least 24 vertical points, usually more) in a similar way to Dong et al. (2019):

$$F_{zi} = F_{zi-1}\left(1 - R_{diss}\left(f\left(\Omega_{zi-1}\right)\right)\frac{z_i - z_{i-1}}{w}\right),$$

where F_{zi} is the mineral flux at depth z_i, R_{diss} is the dissolution rate of the mineral and is a function of the measured mineral saturation state at depth z_{i-1}, and w is the particle sinking rate. For aragonite fluxes (F_{arag}) and dissolution (R_{arag}), we use the aragonite dissolution kinetic rate law generated from in situ data on the same cruise (Dong et al., 2019, Table 2). For calcite fluxes (F_{calc}), we assume that the calcite rain is exclusively foraminifera and coccoliths ($f_{cocco} + f_{foram} = 1$, Table 1). The dissolution rate of coccoliths, R_{cocco}, uses the parameters derived from the data in Figure 3, described in Table 2. The dissolution rate of foraminifera, R_{foram}, is assumed to follow the same functional form as the dissolution rate of coccoliths, R_{cocco}, but dissolves a factor of 1.6 faster, when normalized by mass ($R_{foram} = 1.6R_{cocco}$; Figure 3, Table 2, Section 3.2). This assumption yields a calcite dissolution rate of:

$$R_{calc} = f_{foram}R_{foram} + f_{cocco}R_{cocco};$$

$$= \left(1 - f_{cocco}\right)1.6R_{cocco} + f_{cocco}R_{cocco};$$

$$= \left(1.6 - 0.6f_{cocco}\right)R_{cocco}.$$

Errors in regression parameters were propagated through the dissolution model (shaded envelopes in Figure 3a) by using the linearized log-log fits as "linear model" variables in MATLAB and the "predict" function. Aragonite and calcite fluxes were then summed together to calculate the total PIC flux at each depth.

The appearance of regenerated alkalinity, normalized to the mass of seawater (e.g., Battaglia et al., 2016; Carter et al., 2014, 2021; Feely et al., 2002) is linked to the dissolution of particulate CaCO₃. Although Feely et al. (2002) divided their TA* tracer by 2 to convert into moles of CaCO₃ dissolved, we leave all tracer results in units of
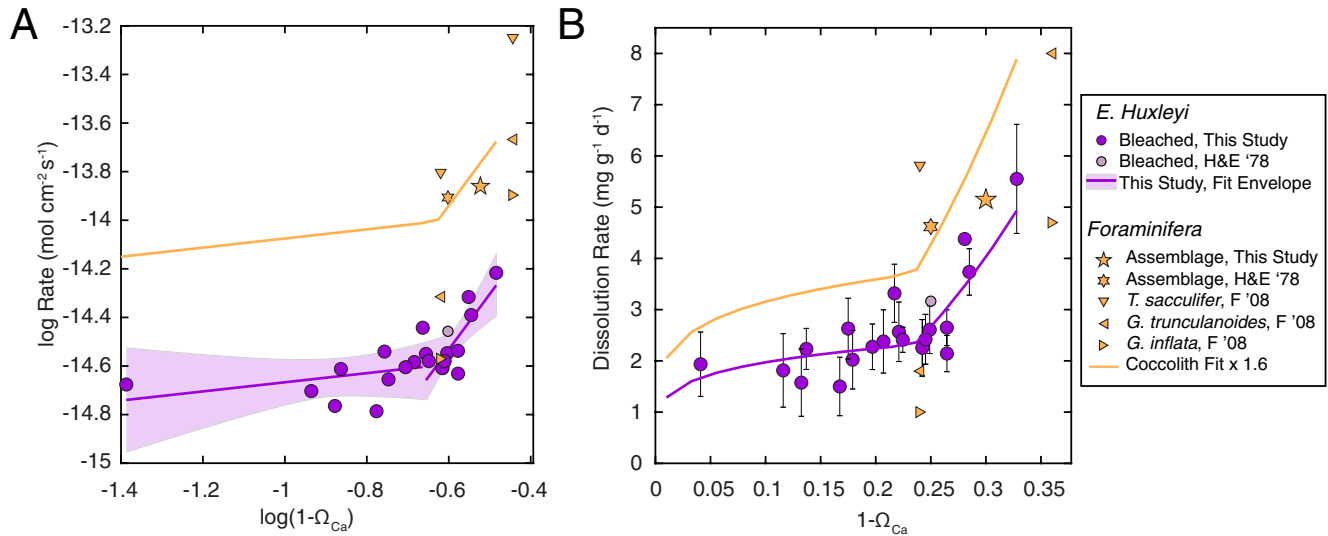
Figure 3. Dissolution rates determined using our custom-built in situ reactors for *E. huxleyi* liths (purple circles), and a planktic foraminifera assemblage (yellow 5-pointed star). (a) Surface-area normalized dissolution rates plotted in logarithmic space. Previous study data are presented for comparison (H&E '78 = Honjo & Erez, 1978; F '08 = Fukuhara et al., 2008). Panel (b) shows the same data as (a) plotted in linear space, normalized by mass only. Regression parameters for the fits are shown in Table 2. The yellow curve shows the coccolith regression with k_{mass} scaled by a factor of 1.6.

alkalinity equivalents per kg of seawater to distinguish between the solid and dissolved sides of the process. It follows that the alkalinity regeneration rate at each depth z, $R_{Alk,zi}$, in units of µmol kg^{-1} yr^{-1}, is calculated as:

$$R_{Alk,zi} = \frac{2 * F_{zi} * R_{diss}\left(f\left(\Omega_{zi}\right)\right)}{\rho w},$$

where ρ is the density of seawater. To account for along-isopycnal mixing, we averaged the R_{Alk} profiles from each of the five stations, binned by potential density (σ_θ) in 0.1 kg m^{-3} bins. This construction yields an approximation of the basin-wide alkalinity regeneration rate profile.

We compared our alkalinity regeneration model to the water column tracer Alk*—derived rates (e.g., Feely et al., 2002). We used GLODAP v2.2019 water chemistry data to calculate both TA* (Feely et al., 2002) and Alk* (Carter et al., 2014), and regressed these quantities against Time Transit Distribution ages (Jeansson et al., 2021, Supporting Information S1 for calculation details). These TTD ages are thought to provide more accurate water mass age estimates than apparent CFC ages, because they take into account a distribution of mixing and other transport processes that can lead to artificially young apparent ages (Sulpis et al., 2021; Waugh et al., 2003).

2.6. Calculation of a Respiratory Effect on Ω

To illustrate the potential effect of locally confined metabolic acidification on saturation state, we assume that organic carbon and CaCO$_3$ are closely associated and packaged together in marine particulate material. It follows that the consumption and degradation of this CaCO$_3$-associated organic matter will drive a localized decrease in saturation state, providing an increased driving force for dissolution. We further assume that this metabolic activity is aerobic, and therefore limited by ambient oxygen concentrations. We make a first attempt at constraining the potential for aerobic metabolism to drive undersaturation and dissolution by "metabolizing" all ambient oxygen and proportionally modifying ambient DIC and alkalinity values in close proximity to particulate CaCO$_3$:

$$DIC_{met} = DIC_{meas} + [O_2]_{meas} * R_{CO};\tag{1a}$$

$$Alk_{met} = Alk_{meas} - [O_2]_{meas} * R_{NO};\tag{1b}$$

$$PO_{4rmet} = PO_{4meas} + [O_2]_{meas} * R_{PO},\tag{1c}$$

where the subscripted "meas" quantities are the reported measurements in the GLODAP v2.2019 database for the North Pacific basin (Olsen et al., 2019). R_{CO}, R_{NO}, and R_{PO} are the Redfield ratios of carbon to oxygen (0.688), nitrate to oxygen (0.0941), and phosphate to oxygen (0.0059), respectively (Anderson & Sarmiento, 1994). We then use DIC_{met}, Alk_{met}, and PO_{4met} to recalculate the Ω influenced by in situ metabolism, Ω_{met} (Figure 2b).

3. Results and Discussion

3.1. Water Column Setting

All water column, sediment trap, and dissolution rate data can be found in the BCO-DMO Data Repository for the CDisK-IV cruise (https://www.bco-dmo.org/project/824992). Figure 2a shows the zonally averaged Pacific water column saturation state, calculated using GLODAP v2.2019 DIC and total alkalinity data. For our CDisK-IV data, we use alkalinity and pH pairs to calculate saturation states that result in systematically lower Ω values throughout the water column (see Naviaux, Subhas, Dong, et al., 2019 for a thorough discussion of this topic). Nevertheless, the trends that we observe are consistent with this zonal mean: a shoaling saturation horizon moving northward, along with a collapsing of the distance between the aragonite and calcite saturation horizons. Figure 2b shows the potential metabolic effect on Ω, demonstrating that Ω_{met} is always lower than ambient Ω (Figure 2a) due to the confined consumption of oxygen and associated production of respiratory CO_2 and/or digestive acids. In general, Ω_{met} is about the same or slightly lower than the ambient aragonite saturation state, that is, the black line in Figure 2b sits at or above the red line in Figure 2a. This calculation is independent of particle size or sinking speed, and metabolism will influence the local saturation state long as metabolic products (e.g., respired CO_2 or digestive acids) are confined in close proximity to particulate $CaCO_3$. We further investigate the relevance of Ω_{met} in Section 3.5.

3.2. Dissolution Rates

The *E. huxleyi* lith data (purple circle) and foraminiferal calcite data (yellow symbols) are presented in Figure 3, and we interpret these data using the framework presented in Figure 1. Panels (a and b) show the same underlying rate data with different normalizations. The surface area-normalized rates are included for those readers most interested in the mechanistic aspects of calcite dissolution (Figure 3a). Chemical oceanographers may find the mass-normalized rates most useful (Figure 3b). The coccolith and foraminifera data are modeled independently, as they are distinct forms of biogenic calcite with well-documented differences in their mineralogy, surface area, and dissolution rate (Honjo & Erez, 1978; Keir, 1980; Subhas et al., 2018). We observe a break in slope in the coccolith data at $\Omega_{critt} = 0.78$ consistent with previous mechanistic determinations and interpretations of Ω_{crit} (Dong et al., 2019; Naviaux, Subhas, Dong, et al., 2019; Naviaux, Subhas, Rollins, et al., 2019; Subhas et al., 2018). We fit *E. huxleyi* dissolution rates in each regime ($1 > \Omega > 0.78$ and $0.78 > \Omega > 0$) to a rate law of the form: $R = k(1-\Omega)^n$. These fits result in a unique set of of $k-n$ values for each regime. Regression parameters for *E. huxleyi* are shown in Table 2, with k values normalized by both mass (k_{mass}) and surface area (k_{sa}).

The calculated *E. huxleyi* n values for both near- and far-from-equilibrium regimes are within error of laboratory values (Table 2). The agreement between laboratory and in situ n values is consistent with previous comparisons between lab and in situ dissolution rates for inorganic calcite and aragonite (Dong et al., 2019; Naviaux, Subhas, Dong, et al., 2019). Although the *E. huxleyi* n values are consistent between laboratory and in situ experiments, the absolute *E. huxleyi* in situ dissolution rates are ~10× slower than those measured in the laboratory, leading to k values that are about an order of magnitude lower than lab-determined k values (Table 2).

There are two potential drivers of slow in situ rates. First, low in situ temperature leads to slower dissolution kinetics (Naviaux, Subhas, Rollins, et al., 2019), so we should expect our in situ rates (determined at 2.4–4.8°C) to be slower than laboratory rates (determined at 21°C). Second, adsorption of naturally occurring dissolved organic carbon (DOC) onto the calcite surface was shown to inhibit calcite dissolution in the ocean by a factor of ~4 (Naviaux, Subhas, Dong, et al., 2019). Combined, the temperature and DOC effects explain the factor of 10 decreased dissolution rate across the entire saturation range measured here (Figure 3, Table 2). The single previous *E. huxleyi* dissolution rate measurement from the Atlantic basin fits well within our more complete data set, suggesting that these rate parameters are broadly applicable to *E. huxleyi* dissolution rates in the ocean (Figure 3 light green circle, Honjo & Erez, 1978).
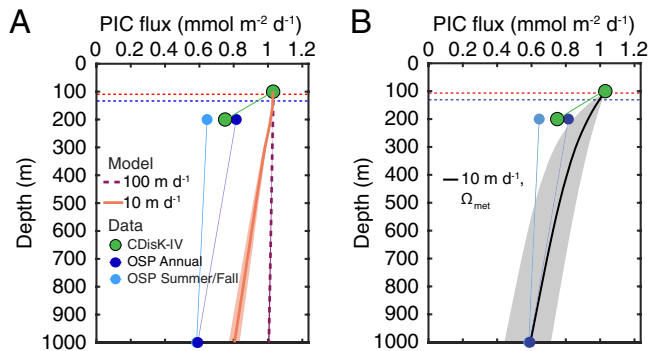
Figure 4. Particulate inorganic carbon (PIC) flux generated by the particle sinking model run at Station 5, close to Ocean Station Papa (OSP). The aragonite and calcite saturation horizons are located at 102 m (red dotted line) and 128 m (blue dotted line), respectively. (a) Model results are shown for a sinking rate of 100 m d^{-1} (purple dashed line) and 10 m d^{-1} (orange line). Model results are compared to our 100 and 200 m PIC fluxes (green points); Summer-Fall OSP fluxes (dark blue points, Timothy et al., 2013), and Annual OSP fluxes (light blue points, Wong et al., 1999). (b) Model results driven by Ω_{met} (solid black line) are compared to the same sediment trap data shown in panel (a).

Our single planktic foraminiferal assemblage dissolution rate is broadly consistent with the sparse and foraminiferal data from the North Atlantic and the Pacific (Fukuhara et al., 2008; Honjo & Erez, 1978, Figure 3). The larger spread in foraminiferal dissolution rates at a given $1-\Omega$ makes it difficult to fit a curve to these data, and this range in reactivity may be related to foraminiferal calcite Mg content (Subhas, McCorkle, et al., 2019). In the absence of more foraminiferal data, we rely on the observation that foraminifera appear to dissolve ~60% (1.6×) faster than coccoliths per unit mass (Chiu & Broecker, 2008; Subhas et al., 2018; Subhas, McCorkle, et al., 2019). Multiplying the near- and far-from-equilibrium *E. huxleyi* k_{mass} values by 1.6 does a reasonable job of approximating the sparse foraminiferal data (Figure 3, yellow line, Table 2). We use this factor of 1.6 in the sinking-dissolution model formulation (Section 2.4). The resulting far-from-equilibrium $\log k_{sa}$ (-12.8 ± 0.3 mol cm^{-2} s^{-1}) is encouragingly consistent with previous determinations of foraminiferal calcite dissolution ($-12.5 < \log k_{sa} < -13.2$ mol cm^{-2} s^{-1}, Gehlen et al., 2005). Despite the large range in foraminiferal dissolution rates, our use of the approximated foraminiferal dissolution rate curve likely does not contribute to a large uncertainty in water column calcite dissolution rates, because foraminifera only comprise 1%–10% of the calcite production (and thus water column calcite dissolution) across the entire transect (Table 1, Ziveri et al., 2022).

These new in situ data suggest slow mass-normalized dissolution rates (<1% per day, Figure 3b) across the entire range of saturation states, slower than some previous parameterizations of dissolution rate (Battaglia et al., 2016; Friis et al., 2006). Given the agreement between these new results and previous biogenic data, and the further agreement between studies of in situ and laboratory inorganic calcite dissolution (Naviaux, Subhas, Dong, et al., 2019), we suggest our rate law parameters (Table 2) can be used to model the dissolution behavior of these select biogenic phases in the ocean. Furthermore, they bear out the decades-old observation that calcite dissolution is slow, and relatively invariant, until Ω drops below Ω_{crit} (Honjo & Erez, 1978; Peterson, 1966).

3.3. A 1D Model of CaCO$_3$ Export and Dissolution

Although previous studies did not assign significance to the functional form and magnitude of dissolution rate constants (e.g., Battaglia et al., 2016; Greenwood, 2009), the direct quantification of in situ CaCO$_3$ dissolution rates presented here and elsewhere (Adkins et al., 2021; Dong et al., 2019; Naviaux, Subhas, Dong, et al., 2019) remove one source of uncertainty in the modeling of carbonate mineral dissolution in the ocean. Combined with calcifier ecology and export, we are now equipped to ask whether these dissolution rates can explain tracer-based and solid-phase dissolution signals in the North Pacific water column.

To understand the magnitude of dissolution, we first ask how much, and what type, of CaCO$_3$ is being produced and exported. A documented northward increase of CaCO$_3$ production and export across the North Pacific reflects the ecological shift between limited (low-CaCO$_3$) picophytoplankton production in the oligotrophic subtropics, and high, coccolithophore- and diatom-dominated, high-CaCO$_3$ production in the subpolar region (Table 1, Dong et al., 2019; Endo et al., 2018; Hou et al., 2019; Juranek et al., 2012). We found that calcite production is overwhelmingly dominated by coccolithophores across the entire transect (Table 1, Ziveri et al., 2022). Although the subtropical CaCO$_3$ export flux contains a large fraction of aragonite (Dong et al., 2019), CaCO$_3$ export is highest in the subpolar gyre and is >90% calcite (Dong et al., 2019). Our Station 1 and Station 5 floating trap fluxes fall within the range of fluxes - and close to the mean values - measured at the Hawaii Ocean Timeseries and Ocean Station Papa (OSP) long-term monitoring stations, respectively (Figure S2 in Supporting Information S1). We acknowledge that our sediment trap fluxes are a single point in time; future work could focus on increasing the number of shallow PIC flux observations, and the construction of a seasonally resolved particulate export model.

We compare our sinking-dissolution model results from Station 5 to historical data from OSP (Figure 4, Figures S3 and S4 in Supporting Information S1). The aragonite and calcite saturation horizons (red and blue horizontal lines, respectively) are very shallow at Station 5 such that CaCO$_3$ will start dissolving soon after organisms die
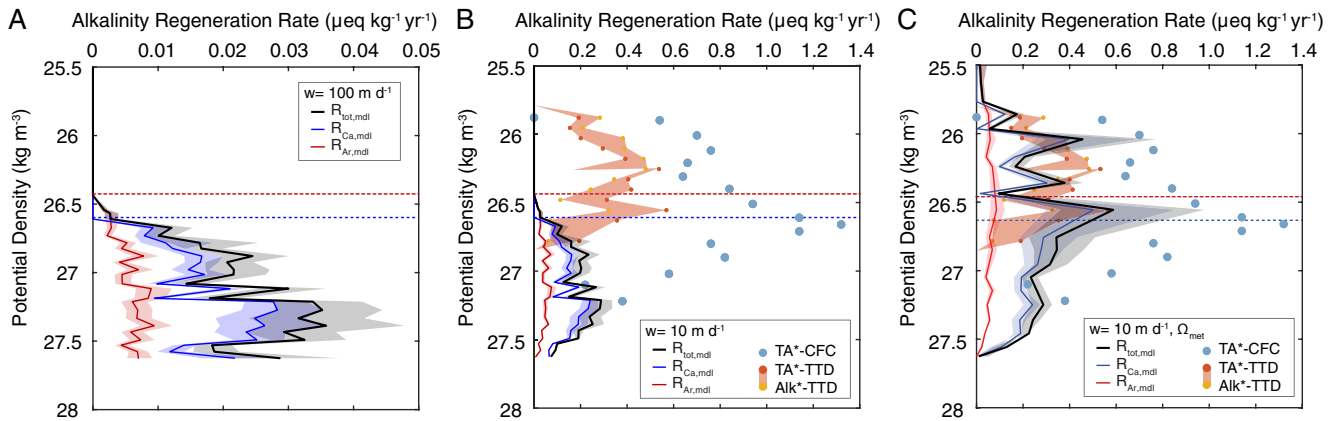
Figure 5. Basin-wide alkalinity regeneration rates estimated by the sinking-dissolution model, binned and averaged over all 5 stations at 0.05 kg m^{-3} potential density intervals. Panel (a) shows our model run at a sinking rate of 100 m d^{-1} (lines) for calcite (blue) aragonite (red) and total CaCO$_3$ (black). Horizontal dashed red and blue lines indicate the shallowest depth at which aragonite and calcite become undersaturated in the section, respectively, denoting the depth at which thermodynamically controlled dissolution begins. Panel (b) shows our model run for a sinking rate of 10 m d^{-1}. Note the change in x-axis scale. North Pacific excess alkalinity-based rates from Feely et al. (2002) (blue points), and new calculated rates using TTD ages (Jeansson et al., 2021) combined with TA* (Feely et al., 2002) and Alk* (Carter et al., 2014), are plotted for comparison, multiplied by two to convert back to alkalinity regeneration rates. The orange envelope shows the range in these TTD-based estimates. (c) Results from the PIC sinking-dissolution model run at a sinking rate of 10 m d^{-1} and driven by Ω_{met} rather than $\Omega_{ambient}$.

and begin to sink through the water column. As do historical OSP fluxes, our sediment trap PIC data demonstrate a strong attenuation in the upper 200 m (Figure 4, Dong et al., 2019; Timothy et al., 2013; Wong et al., 1999). In contrast, running the model with a canonical sinking rate of 100 m d^{-1} dissolves so little CaCO$_3$ that the sinking flux is essentially constant in the upper 1,000 m (dashed purple line, Figure 4a). The flux at 4,000 m is almost identical to the surface flux (Figure S4a in Supporting Information S1), indicating that our dissolution rates, combined with a sinking rate of 100 m d^{-1}, generates minimal dissolution over the entire water column. As an end-member case, reducing the sinking rate to 10 m d^{-1} dissolves ~0.2 mmol CaCO$_3$ m^{-2} d^{-1} in the upper 1,000 m (solid orange line, Figure 4a). The resulting modeled PIC export is still higher at all depths than seasonal and annual sediment trap fluxes. The model also cannot reproduce PIC fluxes from a high-resolution shallow sediment trap array deployment at OSP (Wong et al., 1999, Figure S4b in Supporting Information S1). Regardless of sinking rate, CaCO$_3$ dissolution driven by ambient water-column Ω is simply not fast enough to explain solid-phase PIC loss (Greenwood, 2009; Jansen et al., 2002).

Complementing the solid-phase results, Figure 5 shows basin-wide calcite (blue), aragonite (red), and total (black) alkalinity regeneration rate profiles for a sinking rate of 100 m d^{-1} (Figure 5a) and 10 m d^{-1} (Figure 5b). Model estimates are compared to the TA*-CFC derived rates of Feely et al. (2002) and to the TA*-Alk*-TTD derived rates (blue points and orange shaded regions, respectively, Figure 5b). A model sinking rate of 100 m d^{-1} produces a steadily increasing alkalinity regeneration rate as a function of potential density (Figure 5a). The resulting deep-ocean regeneration rates are very slow, and while they are similar in magnitude to previous estimates of deep-water dissolution rates (0.006–0.05 μmol CaCO$_3$ kg^{-1} yr^{-1}, or 0.012–0.1 μeq TA* kg^{-1} yr^{-1}, Feely et al., 2002), they are about an order of magnitude slower than TA*-based rate estimates at $\sigma_\theta < 27.5$. The dissolution profile modeled with a reduced sinking rate of 10 m d^{-1} (Figure 5b) is about 5× slower than the TA*-CFC rates, but is similar in magnitude to the TTD-based rates. As with the solid-phase comparison, driving the model with ambient Ω cannot produce enough alkalinity to match observations, nor can it produce alkalinity above the saturation horizon.

Aragonite is often suggested as a potential driver of shallow dissolution due to its greater solubility (Feely et al., 2002). We explicitly include aragonite export and dissolution in our model, and yet calcite dissolution regenerates most of the alkalinity at all density classes except for the shallowest isopycnals where only aragonite is undersaturated (Figure 5). Aragonite represents a small fraction of the total modeled dissolution flux and alkalinity regeneration rate, for the following reasons: (a) Calcite dominates the CaCO$_3$ export flux in the subpolar gyre (Dong et al., 2019); (b) The aragonite saturation horizon is only ~50–200 m shallower than the calcite saturation horizon (Figure S5 in Supporting Information S1), meaning that calcite and aragonite begin to

dissolve at close to the same depth and thus at the same time; (c) At the same degree of undersaturation, aragonite dissolves more slowly than calcite because of its low reaction order and rate constant (Table 2, Dong et al., 2019). As evidence for their slow dissolution kinetics (and/or fast sinking rate), aragonite particles are found at depths of 4,000 m in highly undersaturated subtropical waters (Boeuf et al., 2019; Dong et al., 2019).

Our model results demonstrate that $CaCO_3$ dissolution rates driven by ambient Ω, combined with best estimates of calcifier ecology, production, and export, cannot generate the location or magnitude of dissolution signals observed in the shallow ocean, either in the dissolved or particulate phase (Figures 4 and 5). One reason for the data-model mismatch may be our simple treatment of particle dynamics. Large particles make up a majority of export and sink quickly, but smaller sized, slow-sinking particles constitute a majority of particle number and mass (Guidi et al., 2008). Our use of a very slow average sinking rate (10 m d^{-1}) is an end-member attempt at capturing the dissolution rate of both the sinking and suspended pools. However, even slowing sinking rates down to 10 m d^{-1} does not bring our model into agreement with sediment trap fluxes or alkalinity regeneration rates.

Particle formation and destruction processes are likely important for PIC dynamics and export. For instance, Lam et al. (2018) documented a consistent decrease in small size fraction [PIC] directly below the euphotic zone indicating aggregation of smaller material into larger particles, followed by an increase in [PIC] below this depth around 500 m, indicative of disaggregation. Similarly, Dong et al. (2019) showed a "bullseye" pattern of small size fraction [PIC] between ∼200 and 800 m in the N. Pacific. These patterns suggest a net transfer of PIC from larger (sinking) particle sizes to smaller (suspended) ones due to disaggregation in the mesopelagic, and that a nontrivial amount of PIC is either slowly sinking or effectively non-sinking. Indeed, individual coccoliths and spheres sink very slowly, sometimes <1 m d^{-1} (Honjo, 1976; Rosas-Navarro et al., 2018; Zhang et al., 2018). Most importantly, disaggregation in the mesopelagic is thought to be driven by biological processes such as zooplankton grazing and microbial respiration (Burd & Jackson, 2009; Stemmann et al., 2004). For example, particulate barium demonstrates a similar subsurface maximum to PIC that is interpreted as the disaggregation of particles due to biological processing of sinking and suspended material (Bishop, 1988; Bishop & Wood, 2008). In addition to transferring material between the sinking and suspended pools, these biological processes may lead to locally decreased saturation states with respect to ambient seawater via metabolic activity (e.g., Figure 2b), and thus can provide a mechanism to couple the dissolution of $CaCO_3$ to the packaging and cycling of organic carbon.

3.4. Water Column Chemistry Analysis

Our water column data set allows us to investigate the coupling of shallow $CaCO_3$ dissolution to organic carbon remineralization across the North Pacific basin. Previous basin-wide estimates of dissolution rates were estimated using alkalinity-based tracers that are sensitive to $CaCO_3$ production and dissolution (TA*, Feely et al., 2002; Alk*, Carter et al., 2014). We complement this approach by using DIC, $\delta^{13}C$, Apparent Oxygen Utilization (AOU), and pH relationships to identify the balance of organic matter respiration and $CaCO_3$ dissolution in the shallow North Pacific (Figure 6). We focused our examination on a single water mass, North Pacific Intermediate Water (NPIW, Figure S6 in Supporting Information S1, Talley, 1993) to minimize the impact of water mass mixing on seawater properties. Subsetting the data in this way eliminated all data points from Station 5 and left only two data points from below the calcite saturation horizon, but all points fall within the zone of potential metabolic undersaturation (yellow stars, Figure 1).

The regression of 1/DIC versus its $\delta^{13}C$ defines a "Keeling Plot" (Pataki et al., 2003) where the intercept represents the isotopic composition of DIC being added to that water mass ($\delta^{13}C_{add}$), from a combination of oxic respiration and carbonate dissolution. In this simple treatment, we assume end member $\delta^{13}C$ values for organic carbon and calcium carbonate of −23.1‰ and +1‰ respectively, constrained by the composition of our sediment trap material. Assuming two end-member mixing ($f_{org} + f_{carb} = 1$) and rearranging for f_{org}, we recover the equation:

$$f_{org,^{13}C} = \frac{\delta^{13}C_{add} - \delta^{13}C_{carb}}{\delta^{13}C_{org} - \delta^{13}C_{carb}} = \frac{\delta^{13}C_{add} - 1}{-24.1}. \tag{2}$$

The intercept shown in Figure 6a of −6.7‰ translates to an $f_{org,^{13}C}$ of 0.35 for DIC added to NPIW. Performing the same calculation with salinity-normalized DIC gives an intercept of −6.9‰. In other words, this calculation
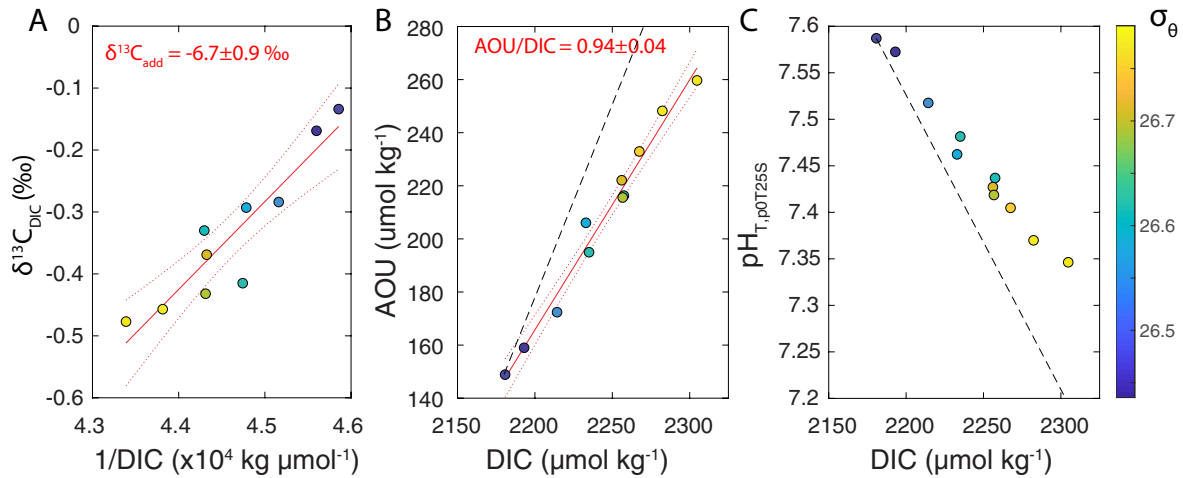
Figure 6. Water mass analysis of the shallow N. Pacific, restricted to North Pacific Intermediate Water identified between Stations 1–4 ($26.4 < \sigma_\theta < 26.8$ and $33.9 < S < 34.1$). The sigma-theta color scale on the right is for all plots. (a) Keeling style plot of inverse dissolved inorganic carbon (DIC) versus $\delta^{13}C$, where the intercept describes the isotopic composition of DIC added to the water mass. The linear regression, uncertainty envelope, and its intercept are shown in red. (b) Apparent Oxygen Utilization versus DIC for the same water mass. The linear regression is shown in red along with its uncertainty envelope and the calculated slope. The black line illustrates the slope of a respiration-only process with a Redfield C:O of 170:116 (Anderson & Sarmiento, 1994). (c) pH (total scale, referenced to 25°C and atmospheric pressure) versus DIC. The black line illustrates the slope of a respiration-only process. The offset between this line and the data suggest buffering.

suggests that only 35% of regenerated DIC is sourced from respiratory CO_2 in NPIW, implying that the other 65% comes from $CaCO_3$ dissolution.

As an independent test, the slopes of AOU versus DIC in this water mass should also trace the fraction of carbon added to the system from oxic respiration (Figure 6b). Recent analyses suggest that AOU is erroneously high in this region (Carter et al., 2021). We circumvent this issue by analyzing the change in AOU rather than its absolute value, and compare it to the change in DIC. Slopes of AOU versus DIC (S_{oc}), that is, the change in AOU per unit change in DIC, were calculated to assess the fraction of organic carbon:

$$f_{org,AOU} = \frac{\Delta DIC_{org}}{\Delta DIC_{tot}} = \frac{\Delta AOU}{\Delta DIC_{tot}} \cdot \frac{C_{org}}{O_2}\bigg|_{Redfield} = S_{oc} \cdot \frac{117}{170}, \tag{3}$$

where $-O_2/C_{org} = 170/117 = 1.47 \pm 0.19$ based on the global variation in this ratio suggested by Anderson and Sarmiento (1994). The large error envelope used encompasses the historical "Redfield" ratio of $138/106 = 1.30$. This regression gives an S_{oc} of 0.94, well below any $-O_2/C_{org}$ remineralization ratio estimate. Substituting this value into Equation 3 yields an $f_{org,AOU}$ of 0.65 ± 0.08, significantly higher than the f_{org} recovered from isotope balance (0.35), but still much lower than 100%. As a third independent measure, our measured NPIW pH decreases from 7.58 to 7.32 over the range of DIC addition. DIC generated solely from oxic respiration would drive pH much lower, to 7.21 (Figures 2 and 6c, SI methods), demonstrating that pH buffering of respiratory CO_2 is occurring in NPIW.

Complicating these interpretations is the invasion of anthropogenic CO_2, which increases the amount of DIC and decreases its isotopic composition (i.e., the Suess Effect). We did not measure transient tracer concentrations (e.g., CFC-12 and SF_6) on our CDisK-IV cruise but we used recent GOSHIP North Pacific data to estimate the invasion of Anthropogenic CO_2 along the P16 transect and its influence on the $\delta^{13}C$, DIC, and AOU relationships presented here. Cruise information and calculations are shown in Table S1 and Figure S7 of Supporting Information S1, and follow established protocols (Eide, Olsen, Ninnemann, & Eldevik, 2017; Eide, Olsen, Ninnemann, & Johannessen, 2017).

Keeling plots and AOU:DIC analysis for these recalculations are compared to our CDisK-IV cruise data in Figure 7. After correction for anthropogenic CO_2, a regression-based $\delta^{13}C_{add}$ value of -12.8 ± 0.5‰ for the three GOSHIP cruises corresponds to an f_{org} of $56 \pm 5\%$ for the DIC budget of NPIW (Figure 7a). The AOU:DIC slope in our data is similarly adjusted (Figure 7b), giving an f_{org} of $59 \pm 8\%$ for NPIW DIC. We note that the
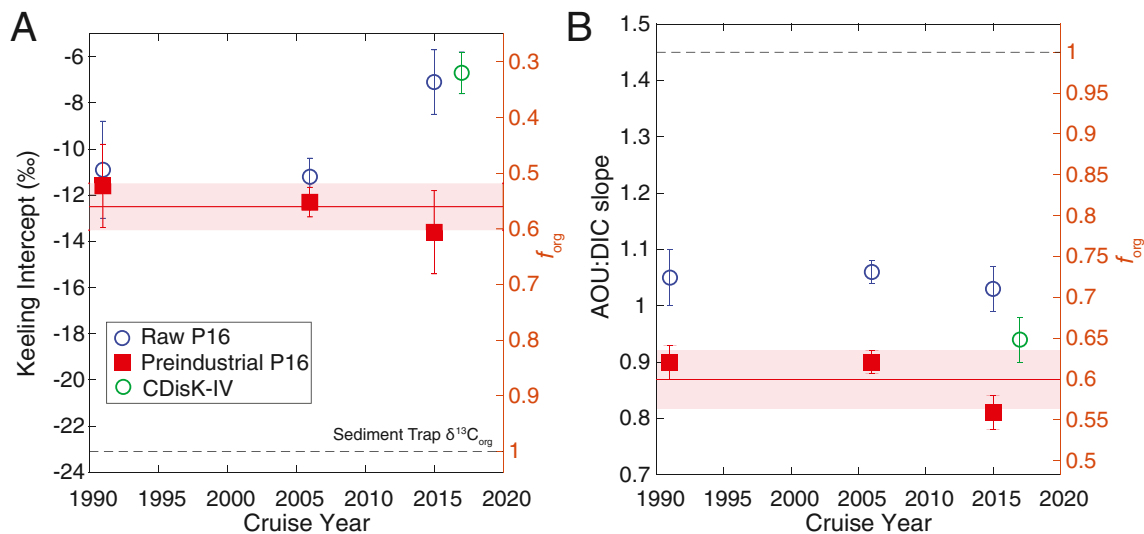
Figure 7. Keeling intercepts and AOU:DIC slopes for the P16 cruises and the 2017 CDisK-IV cruise. Preindustrial calculations were made as described in the SI text. The Keeling intercepts do not change significantly between each cruise, and our 2017 intercept is identical to the intercept measured on raw 2015 P16 data. The AOU:DIC relationships show a broadly similar pattern, although AOU:DIC may be shifting toward lower values through time. We do not interpret this change here, as we cannot unequivocally diagnose the same change in the ^{13}C balance.

Suess effect and AOU:DIC corrections go in opposite directions (flipped right-hand axes in Figures 7a and 7b). This is because the Suess Effect outweighs the accumulation of anthropogenic DIC, whereas for AOU:DIC, the AOU is unaffected and the DIC gradient shrinks. Therefore, anthropogenic CO_2 correction adjusts these independent estimates in opposite directions, bringing them into excellent agreement with a consistent, average f_{org} of 57 ± 8%. In terms of the contribution of $CaCO_3$ ($1-f_{org}$), we find 43% ± 8% of regenerated DIC is sourced from $CaCO_3$ dissolution in a water mass that exists almost exclusively above the calcite saturation horizon. The consistency of this signal over time in all of the P16 data from the last 30 years implies that dissolution in waters that are clearly supersaturated with respect to calcite is a fundamental component of the shallow carbon cycle in the North Pacific.

3.5. Modeling Metabolically Driven CaCO₃ Dissolution

These analyses bring into question the utility of relating $CaCO_3$ dissolution to ambient water column saturation state. We tested the effect of metabolic activity on shallow $CaCO_3$ dissolution by running our sinking-dissolution model with Ω_{met} instead of ambient Ω (i.e., using Figure 2b, rather than Figure 2a, as the driving force for dissolution). While we do not suggest that oxygen is fully consumed within confined environments such as particle aggregates or zooplankton guts, this calculation illustrates the possibility of metabolic dissolution in the mesopelagic North Pacific and gives a maximum rate by assuming all O_2 is consumed. We again use the 10 m d^{-1} sinking rate as an end-member attempt to capture the dynamics of the entire PIC pool, with the assumption being that metabolic activity can influence all particle sizes regardless of sinking speed. Running the model in this configuration generates enough dissolution to match the 1,000 m sinking flux, although it still overpredicts the 200 m flux (Figure 4b). The complement to this calculation is a comparison of our model to observations of alkalinity regeneration in the North Pacific. Driving the model with Ω_{met} generates basin-wide alkalinity at the same density classes that demonstrate excess alkalinity above the saturation horizon, and even shows the two peaks in alkalinity regeneration at $\sigma_\theta \sim 26$ and 26.54 (Figure 5c). These model results are in quantitative agreement with Alk*-TTD regeneration rate estimates, with alkalinity regeneration initiating at $\sigma_\theta \sim 25.8$ and reaching a maximum rate of ~0.6 ueq kg^{-1} yr^{-1}.

Our water column data allow us to interrogate the mechanisms behind the shape and magnitude of alkalinity regeneration rates. The overall magnitude of the signal is driven by high transition zone and Subpolar $CaCO_3$ export at Stations 4 and 5 (Figure 4b and Figure S8b in Supporting Information S1). The shallowest alkalinity
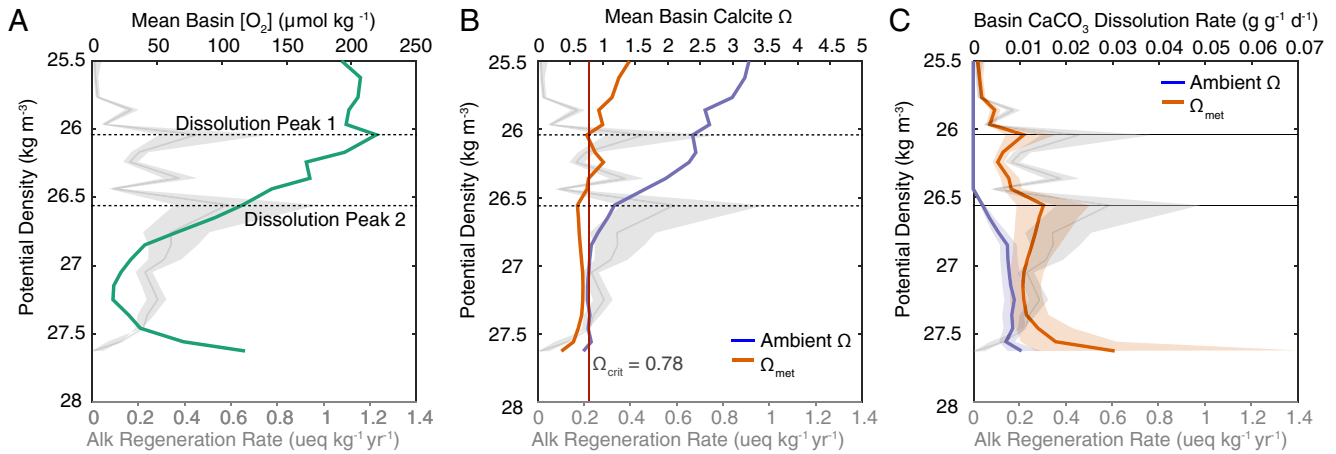
Figure 8. Water column data from the CDisK-IV cruise, binned and averaged by potential density. Alkalinity regeneration rates from Figure 9 are shown in the background and on the bottom axis. (a) Mean oxygen profile, demonstrating a well-ventilated peak at the same location as the peak in dissolution (Peak 1). (b) Ambient (purple) and respiration-driven (orange) calcite saturation state, with the same dissolution rate profile shaded for comparison. The first peak in dissolution represents the first time that Ω_{met} drops below $\Omega_{crit} = 0.78$. Panel (c) shows the $CaCO_3$ dissolution rate generated by either Ambient Ω or Ω_{met}, showing the two peaks in dissolution generated by shallow Ω_{met} dropping below $\Omega_{crit} = 0.78$.

regeneration peak is driven not from particularly low ambient saturation state, but from recently ventilated, high oxygen subpolar gyre waters (Figure 8a and Figure S8 in Supporting Information S1) across this range of density classes above the ambient saturation horizon. Shallow North Pacific waters become denser at higher latitudes, and the $\sigma_\theta \sim 26$ and 26.54 density demonstrate a strong influence of O_2-rich Subpolar waters (Figure S8a in Supporting Information S1). At $\sigma_\theta = 26$ this high O_2 is able to drive Ω_{met} below Ω_{crit} (0.78, Table 2, Figures 3 and 8b), generating a rapid increase in dissolution rate because of the mechanistic rate transition from step-edge to homogenous 2D dissolution (Adkins et al., 2021, Figures 3a and 8c). The second peak at $\sigma_\theta = 26.54$ is generated by a local minimum in Ω_{met}, through a combination of low ambient Ω and relatively high O_2. Below this peak, modeled alkalinity generation decreases because even though dissolution rates are fast (Figure 8c), the PIC flux is strongly attenuated by this point.

The envelope of our modeled dissolution rates appears to overpredict dissolution in the deeper ocean below $\sigma_\theta = 26.75$, likely because the model maintains a constant, slow sinking rate throughout the water column. This is unrealistic and contrary to sediment trap sinking rate observations that generally record an increase in sinking rate with depth (Berelson, 2001). Instead, after passage through the upper water column and the Twilight Zone, PIC is likely delivered rapidly to the sediment-water interface where, in the case of the North Pacific, it dissolves before it is buried (Berelson et al., 2007; Feely et al., 2002; Timothy et al., 2013).

3.6. Dissolved and Solid-Phase Evidence for Shallow $CaCO_3$ Cycling

The appearance of alkalinity above the saturation horizon is undisputed (Battaglia et al., 2016; Carter et al., 2021; Feely et al., 2002; Sulpis et al., 2021), but attempts to transform these tracer observations into models of the calcium carbonate cycle have proven difficult. Models of the $CaCO_3$ cycle, while broadly similar to observations, cannot match TA*, and TA*-CFC observations in detail due to uncertainties in the modeled distribution of saturation state, water circulation, $CaCO_3$ production, and until now, $CaCO_3$ dissolution rate (Battaglia et al., 2016; Dunne et al., 2012; Friis et al., 2006). These uncertainties have left models with no mechanistic explanation for the apparent decoupling of dissolution rate and ambient saturation state (e.g., Battaglia et al., 2016; Carter et al., 2021).

In this work the combination of a complete understanding of the physical chemistry of dissolution, the measured rates and polymorph partitioning of $CaCO_3$ production, and the presence of high $[O_2]$ along shallow isopycnals is able to reproduce the two peaks in alkalinity regeneration observed by Feely et al. (2002) and the magnitude of TA*-TTD age-based rates (Figure 5c, Sulpis et al., 2021). We attribute the peaked structure of dissolution as

a function of seawater density to an interplay between ambient saturation state, metabolic oxygen consumption, and the mechanistic rate transition at $\Omega_{critical} = 0.78$ (Figures 5c and 8). Modeled peaks are generally sharper than the TA*-CFC features (Figure 6c), suggesting that diapycnal mixing could smooth and broaden locally generated signals across potential density surfaces.

Water mass transport more generally is a nontrivial consideration, especially in the North Pacific (Holzer et al., 2021). Studies using updated estimates of water mass age and transport have all found slower alkalinity regeneration rates compared to the original TA*-CFC approach, due to mixing effects on CFC distributions (Battaglia et al., 2016; Carter et al., 2021; Feely et al., 2002; Sulpis et al., 2021). Alkalinity produced on the shelves or in the deep ocean, and its subsequent transport to the mesopelagic, could also lead to artificially high estimates of shallow dissolution (Battaglia et al., 2016; Friis et al., 2006). However, the similarity between our model results and Alk*-TTD analyses suggest that in situ metabolic $CaCO_3$ dissolution is the primary source of alkalinity accumulating in the mesopelagic North Pacific. In Text S9 in Supporting Information S1 we present simple calculations that suggest transport is a secondary, rather than primary, contributor to shallow alkalinity anomalies. The ideal approach to studying this transport issue is to embed updated dissolution rate equations (Table 2) within an ocean circulation and biogeochemistry model; ideally with accurate representations of shelf alkalinity sources; aggregation/disaggregation; microbial respiration; and zooplankton grazing processes. We leave this effort for future work.

Attribution of an excess alkalinity signal above the saturation horizon solely to transport ignores the substantial and growing body of solid-phase evidence for rapid $CaCO_3$ dissolution across multiple oceanic regimes. From 0 to 55° N in the Atlantic Ocean, particulate $CaCO_3$ declines between 200 and 1,000 m, well above the calcite saturation horizon (Barrett et al., 2014). Using a mean PIC turnover time of 10 days, these authors calculated dissolution rates of 0.2 and 0.9 mmol m^{-2} d^{-1} in the subpolar and subtropical North Atlantic, respectively. Sediment trap PIC fluxes also attenuate by ∼1 mmol m^{-2} d^{-1} in the upper 200m at the coccolithophore-dominated Porcupine Abyssal Plain in the Subpolar North Atlantic (Marsay et al., 2015), suggesting substantial shallow dissolution. Shallow dissolution of particulate $CaCO_3$ is of course also observed in the North Pacific. The particulate $CaCO_3$ inventory from 50 to 500 m water depth at Station K2 in the Northwest Pacific decreased by 70%–90% over a 10-day period, corresponding to a dissolution rate of 1.1 mmol PIC m^{-2} d^{-1} (Bishop & Wood, 2008). The vertical reductions in shallow PIC flux at OSP are most pronounced at times of high $CaCO_3$ production and export, suggesting a coupling between biological activity and dissolution (Timothy et al., 2013). Our own CDisK-IV PIC fluxes decrease between 100 and 200 m in most of the trap deployments across the North Pacific (Table 1), and PIC flux attenuations show a stronger correlation to the attenuation of POC flux (Dong et al., 2019) than to ambient saturation state (Figure S9 in Supporting Information S1). The results and analyses presented here, combined with the above suite of historical observations, point toward the presence of a shallow calcium carbonate cycle: One that cannot be driven by ambient Ω, or sustained by more soluble phases like aragonite.

3.7. The Role of Metabolic Activity on Shallow $CaCO_3$ Dissolution

The influence of metabolism on $CaCO_3$ dissolution provides a mechanism for coupling solid-phase and tracer observations. The earliest evidence of respiration-driven dissolution comes from porewaters, where the products of oxic respiration build up due to diffusive limitation, leading to lower saturation states relative to the overlying bottom water (Emerson & Archer, 1990; Emerson & Bender, 1981; McCorkle & Emerson, 1988; Steiner et al., 2019). By analogy, the two locations that may exhibit decreased saturation state in the water column are the oxygen-depleted interiors of marine snow aggregates and the digestive tracts of zooplankton (Alldredge & Cohen, 1987; Pond et al., 1995).

Particulate microenvironments are implicated in a number of globally relevant oceanographic processes that require the drawdown of O_2 to suboxic or anoxic levels (Babbin et al., 2015; Bianchi et al., 2018). The depletion of oxygen within particle interiors requires respiration of organic carbon and therefore the buildup of respiratory CO_2, which will depress saturation state and cause $CaCO_3$ dissolution (Figure 2b). We tested this hypothesis by re-analyzing pH and O_2 microelectrode profiles inside marine snow aggregates containing coccolithophores (Alldredge & Cohen, 1987). If respiration were the only process occurring in these aggregates, the gradient in O_2 depletion between ambient seawater and the particle interior should produce a steady-state respiratory CO_2 gradient that can be translated into the observed steady-state pH gradient. This approach is conceptually similar
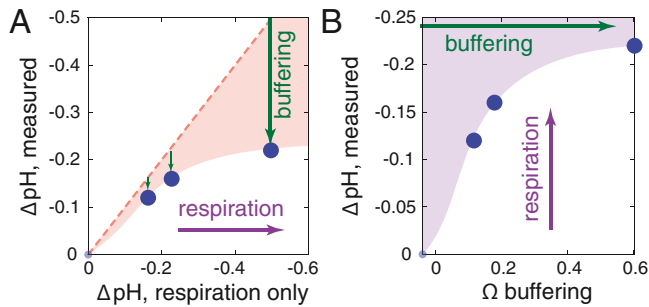
Figure 9. Reanalysis of microelectrode data from three marine snow aggregates from Alldredge and Cohen (1987). (a) The ΔpH expected from oxic respiration (dashed line) was estimated by converting ΔO_2 to ΔCO_2, and then to ΔpH (see main text and Supporting Information S1 for details). In all three particles, measured ΔpH is less than the respiration-only ΔpH. These data suggest a buffering of pH (green arrows) within the marine snow aggregates. (b) The amount of Ω buffering calculated by differencing the saturation states estimated from oxygen-extrapolated and measured pH gradients, as a function of the measured pH gradient. There is more buffering at higher ΔpH.

to Section 2.5 and Figure 2b, but comparing pH instead of Ω (Text S3 in Supporting Information S1 for details). We analyzed pH and oxygen data for three marine snow aggregates that experienced at most a 46% depletion in oxygen. We avoided the anoxic fecal pellets because of anoxic reactions that can change the DIC/Alkalinity/pH balance above and beyond oxic respiration and $CaCO_3$ dissolution (e.g., sulfate reduction, Berner et al., 1970). In all three particles for which pH and O_2 profiles exist, the measured ΔpH is much smaller than ΔpH estimated from oxic respiration alone (Figure 9a), suggesting that particles may serve as the locus for pH buffering of respired CO_2 via $CaCO_3$ dissolution. Figure 9b shows the difference between saturation state calculated from the measured ΔO_2 and measured ΔpH. Buffering is elevated at high oxygen drawdown, which may impact the efficiency of this buffering reaction: As buffering grows, dissolution slows. At steady state, dissolution must be sustained at a rate that continuously buffers pH changes within the particle aggregate, until either organic carbon or calcium carbonate runs out. These analyses are presented with the caveats that (a) these aggregates were coastal in origin and may not represent open-ocean particle composition and (b) the fluid dynamics in this experimental setup are meant to simulate, but not reproduce, the conditions experienced by an in situ aggregate. We acknowledge that large aggregates capable of sustaining O_2 and pH gradients sink more quickly than the 10 m d^{-1} modeled rate above (Figures 4b, 5c, and 8). Without better constraints on size-sinking-dissolution relationships, the contribution of aggregates to the total shallow dissolution flux is poorly constrained.

Although we have not explicitly modeled zooplankton grazing, it may be captured implicitly in the Ω_{met} framework. Zooplankton are abundant in the upper water column and modulate the vertical flux of material in the Twilight Zone through grazing, respiration, and repackaging material into fecal pellets (Bishop & Wood, 2008; Bishop et al., 1986; Henson et al., 2019; Steinberg & Landry, 2014; Steinberg et al., 2008; Stukel et al., 2019; Turner, 2015). Grazing experiments demonstrated that *E. huxleyi* liths dissolve within copepod guts (Harris, 1994), and that the extent of dissolution varies depending on feeding state (White et al., 2018). A numerical model suggested that gut dissolution may account for up to 25% of the total shallow dissolution signal (Jansen & Wolf-Gladrow, 2001), which qualitatively fits with the observed mismatches between our model and the 200m sediment trap data (Figure 4b).

The fact that we require a very slow sinking rate of 10 m d^{-1} may be reconciled by dissolution within zooplankton guts. The Ω_{met} model does not include the production of strong digestive acids that would be more corrosive to $CaCO_3$ than respiratory CO_2 alone (Jansen & Wolf-Gladrow, 2001; Pond et al., 1995). In addition to their direct metabolic influence, zooplankton-produced fecal pellets are usually denser than other types of aggregates (Iversen & Ploug, 2010; Ploug et al., 2008); they can go anoxic (Alldredge & Cohen, 1987; Ploug et al., 1997); and they exhibit lower diffusivities compared to aggregates (Ploug et al., 2008). It is possible that these factors lead to an enhanced coupling of respiration and dissolution in fecal pellets relative to other marine snow aggregates, despite their high density and rapid sinking speeds. Zooplankton are known to disaggregate existing fecal pellets instead of reingesting them (Alldredge et al., 1987; Dilling & Alldredge, 2000; Iversen & Poulsen, 2007), cycling repackaged fecal material through the slow- and non-sinking particulate pool (Fischer & Karakaş, 2009; Lam & Marchal, 2015; Riley et al., 2012). This disaggregated material would have more time to be respired (and dissolved) in the upper water column through sustained metabolic activity.

Finally, mismatches between $CaCO_3$ production and euphotic zone export imply a large dissolution flux higher in the water column within the euphotic zone itself (Ziveri et al., 2022). The influence of zooplankton in the euphotic zone may not be captured by our Ω_{met} framework, because surface saturation states are often too high to be driven undersaturated by oxygen consumption alone (see, e.g., surface Ω_{met} in the subtropics, Figure 2b).

In summary, these studies suggest that particle aggregation coupled to microbial respiration, and zooplankton grazing and subsequent fecal pellet production, are involved in transferring material between the sinking and suspended phases, and in creating the necessary environments to couple metabolic activity to $CaCO_3$ dissolution. Our Ω_{met} model appears to capture large-scale dissolution signals in the mesopelagic, and because zooplankton

are aerobic organisms, we may be capturing the effect of zooplankton grazing without its explicit inclusion in the model. However, we acknowledge that many details are not captured by the assumptions in our simple oxygen drawdown model (i.e., 1:1 oxygen and DIC flushing from the particle interior; complete oxygen drawdown; a 10 m d^{-1} sinking rate; the absence of zooplankton) and likely contribute to the mismatches between our modeled dissolution rates and previous data (Figures 4b and 5c). We suggest that future work focuses on quantifying the unique roles of phytoplankton-derived aggregates versus grazing and fecal pellet microenvironments in mediating calcite dissolution in supersaturated waters.

3.8. A Vigorous Respiration-Driven Shallow Alkalinity Cycle and Its Implications

This study set out to provide solid-phase, dissolved phase, and experimental constraints on the $CaCO_3$ cycle of the North Pacific Ocean. In the process, we have documented an apparent shallow $CaCO_3$ cycle that we hypothesize is driven by metabolic $CaCO_3$ dissolution (Milliman et al., 1999). This mechanism does not emerge by coincidence. Most marine $CaCO_3$ is biogenic, and is precipitated in direct contact with organic material. The consumption of this organic matter therefore directly influences the dissolution of biologically produced $CaCO_3$. It is likely that metabolic activity drives a substantial portion of alkalinity regeneration, both in the water column as shown here, and in shallow and deep ocean sediments (Burdige et al., 2010; Emerson & Archer, 1990; Emerson & Bender, 1981; Steiner et al., 2019). This mechanism also allows for the intimate association of $CaCO_3$ and the enzyme carbonic anhydrase to elevate dissolution rates (Dong, Berelson, Teng, et al., 2020; Subhas et al., 2017; Subhas, Adkins, et al., 2019).

The extent to which $CaCO_3$ and organic carbon export and remineralization are coupled controls the extent to which respired CO_2 is neutralized in the upper ocean. Packaging of $CaCO_3$ with organic carbon promotes $CaCO_3$ dissolution, quickly neutralizing a substantial fraction of respired CO_2. A shallow particulate dissolution flux of 0.5 mmol m^{-2} d^{-1} (0.2 mol m^{-2} yr^{-1}) can be compared with sediment trap-derived organic carbon fluxes in the North Pacific, which generates 0.3–1.2 mol m^{-2} y^{-1} of respiratory CO_2 from 100 to 1,000 m (Martin et al., 1987; Smith et al., 2018; Wong et al., 1999). Dissolution of sinking $CaCO_3$ alone therefore can instantly neutralize approximately 15%–66% of respiratory CO_2 in the shallow ocean, and suspended $CaCO_3$ probably neutralizes even more. Our DI^{13}C, AOU and pH water column data confirm this fraction of neutralization ($\sim$40%).

More soluble forms of $CaCO_3$ remain enigmatic. Pelagic fish produce highly soluble Mg-calcites that may contribute as much as 0.02–0.07 mmol $CaCO_3$ m^{-2} d^{-1} globally (R. W. Wilson et al., 2009), a factor of 7–25 less than the required dissolution flux of $\sim$0.5 mmol m^{-2} d^{-1}. While potentially regionally important, more work is needed to quantify the importance of fish-produced carbonates for the North Pacific $CaCO_3$ budget. However, a similar C_{org}-$CaCO_3$ packaging argument could be made for observations of pteropods dissolving from the inside out: Pteropod shells compartmentalize organic carbon degradation and acid generation, leading to a decrease in saturation state and rapid interior dissolution (Oakes et al., 2019; Peck et al., 2018).

Our study instead suggests that primary coccolith calcite is responsible for a large portion of production and dissolution in the North Pacific. Coccolithophores are blooming organisms and require aggregation for export (Honjo, 1976; Ziveri et al., 2000), driven by a combination of (a) viral infection dynamics leading to bloom crashes and export (Laber et al., 2018); (b) dissolution during digestion (Bishop et al., 1980, 1986; Harris, 1994; White et al., 2018); and (c) grazing leading to dense fecal pellet production and sinking (Iversen & Ploug, 2010). The multiple mechanisms of coccolith $CaCO_3$ aggregation, grazing, and export likely produce a spectrum of particulate size distributions (Cael et al., 2021; Durkin et al., 2015), sinking rates (McDonnell & Buesseler, 2010), respiration rates (Collins et al., 2015; Omand et al., 2020; Ploug, 2001), porosities (Ploug et al., 2008), PIC:POC (Passow & De La Rocha, 2006), and other particle qualities that all determine the potential for shallow dissolution and the subsequent export of $CaCO_3$ and organic carbon out of the mesopelagic.

Finally, selective shallow dissolution of coccolith calcite, driven by particle aggregation and remineralization dynamics, provides a mechanism to reconcile production estimates with the composition of deep ocean $CaCO_3$ fluxes and sedimentary calcite. Coccoliths make up 85%–99% of calcite production in the North Pacific (Table 1, Ziveri et al., 2022), but comprise only $\sim$50% of sedimentary $CaCO_3$ (Broecker & Clark, 2009; Kawahata et al., 2002). Foraminifera may dissolve faster than coccolithophores, but they are large, sink quickly, and contain little POC. Coccoliths, although they dissolve more slowly (Figure 3), are directly implicated in the above aggregation-disaggregation export mechanisms that lead to their selective dissolution in the shallow ocean. Shallow

dissolution therefore acts as a major filter on the composition of sinking $CaCO_3$, and the extent of its influence is likely tied to ecosystem structure the associated styles of carbon export and ballasting, which vary regionally and may not be constant through time.

4. Conclusions

Our research expedition data set, model results, and a suite of historical solid-phase and tracer results, all suggest that shallow dissolution is widespread in the North Pacific Ocean and beyond. Our new data further constrain the source of this feature to coccolith calcite, and the driver of this feature to metabolic activity. The attribution of this mechanism to the widespread occurrence of shallow $CaCO_3$ dissolution provides an explanation for the decoupling of dissolution rate to ambient saturation state, and for a reconciliation between $CaCO_3$ production and sediment composition. This decoupling from in situ Ω is still directly tied to well constrained dissolution rate laws that are fundamentally driven by critical Ω values for the change in dissolution mechanism. Most crucially for the carbon cycle, the coupling of organic and inorganic carbon remineralization means that the partitioning of alkalinity between the shallow and deep oceans is controlled to a substantial extent by a vigorous production-respiration-dissolution cycle in the upper ocean. This shallow alkalinity cycle is likely a fundamental feature of the carbon cycle, and is likely subject to a similar set of controls as the cycle of organic carbon.

Conflict of Interest

The authors declare no conflicts of interest relevant to this study.

Data Availability Statement

The author list represents the entire science party of the CDisK-IV cruise, with the exception of PDQ who contributed GOSHIP data. All authors contributed to data collection and the final manuscript. Work was conceived by JFA, WB, AVS, SD, and JN. Data was analyzed by AVS, JFA, WB, and SD. The manuscript was written by AVS with contributions from all coauthors. Data sets can be found on BCO-DMO including dissolution rate experiments (https://www.bco-dmo.org/dataset/856409), sediment traps (https://www.bco-dmo.org/dataset/860424), McLane pumps (https://www.bco-dmo.org/dataset/860409), and bottle data including full carbonate chemistry, nutrients, density, AOU, and saturation state (https://www.bco-dmo.org/dataset/836954).

References

Adkins, J. F., Naviaux, J. D., Subhas, A. V., Dong, S., & Berelson, W. M. (2021). The dissolution rate of $CaCO_3$ in the ocean. *Annual Review of Marine Science*, *13*(1), 57–80. https://doi.org/10.1146/annurev-marine-041720-092514

Alldredge, A. L., & Cohen, Y. (1987). Can microscale chemical patches persist in the sea? Microelectrode study of marine snow, fecal pellets. *Science*, *235*(4789), 689–691. https://doi.org/10.1126/science.235.4789.689

Alldredge, A. L., Gotschalk, C. C., & MacIntyre, S. (1987). Evidence for sustained residence of macrocrustacean fecal pellets in surface waters off Southern California. *Deep Sea Research Part A. Oceanographic Research Papers*, *34*(9), 1641–1652. https://doi.org/10.1016/0198-0149(87)90113-0

Anderson, L. A., & Sarmiento, J. L. (1994). Redfield ratios of remineralization determined by nutrient data analysis. *Global Biogeochemical Cycles*, *8*(1), 65–80. https://doi.org/10.1029/93gb03318

Archer, D., Kheshgi, H., & Maier-Reimer, E. (1998). Dynamics of fossil fuel CO_2 neutralization by marine $CaCO_3$. *Global Biogeochemical Cycles*, *12*(2), 259–276. https://doi.org/10.1029/98gb00744

Babbin, A. R., Bianchi, D., Jayakumar, A., & Ward, B. B. (2015). Rapid nitrous oxide cycling in the suboxic ocean. *Science*, *348*(6239), 1127–1129. https://doi.org/10.1126/science.aaa8380

Barrett, P. M., Resing, J. A., Buck, N. J., Feely, R. A., Bullister, J. L., Buck, C. S., & Landing, W. M. (2014). Calcium carbonate dissolution in the upper 1000 m of the eastern North Atlantic. *Global Biogeochemical Cycles*, *28*(4), 386–397. https://doi.org/10.1002/(issn)1944-9224

Battaglia, G., Steinacher, M., & Joos, F. (2016). A probabilistic assessment of calcium carbonate export and dissolution in the modern ocean. *Biogeosciences*, *13*(9), 2823–2848. https://doi.org/10.5194/bg-13-2823-2016

Berelson, W. M. (2001). Particle settling rates increase with depth in the ocean. *Deep-Sea Research Part II*, *49*(1–3), 237–251. https://doi.org/10.1016/s0967-0645(01)00102-3

Berelson, W. M., Balch, W. M., Najjar, R., Feely, R. A., Sabine, C., & Lee, K. (2007). Relating estimates of $CaCO_3$ production, export, and dissolution in the water column to measurements of $CaCO_3$ rain into sediment traps and dissolution on the sea floor: A revised global carbonate budget. *Global Biogeochemical Cycles*, *21*(1). https://doi.org/10.1029/2006gb002803

Berner, R. A., & Morse, J. W. (1974). Dissolution kinetics of calcium carbonate in sea water; IV, Theory of calcite dissolution. *American Journal of Science*, *274*(2), 108–134. https://doi.org/10.2475/ajs.274.2.108

Berner, R. A., Scott, M. R., & Thomlinson, C. (1970). Carbonate alkalinity in the pore waters of anoxic marine sediments. *Limnology and Oceanography*, *15*(4), 544–549. https://doi.org/10.4319/lo.1970.15.4.0544

Bianchi, D., Weber, T. S., Kiko, R., & Deutsch, C. (2018). Global niche of marine anaerobic metabolisms expanded by particle microenvironments. *Nature Geoscience*, *11*(4), 263–268. https://doi.org/10.1038/s41561-018-0081-0

Bishop, J. K. B. (1988). The barite-opal-organic carbon association in oceanic particulate matter. *Nature*, *332*(6162), 341–343. https://doi.org/10.1038/332341a0

Bishop, J. K. B., Collier, R. W., Kettens, D. R., & Edmond, J. M. (1980). The chemistry, biology, and vertical flux of particulate matter from the upper 1500 m of the Panama Basin. *Deep Sea Research*, *27*(8), 615–640. https://doi.org/10.1016/0198-0149(80)90077-1

Bishop, J. K. B., Stepien, J. C., & Wiebe, P. H. (1986). Particulate matter distributions, chemistry and flux in the Panama Basin. *Progress in Oceanography*, *17*(1–2), 1–59. https://doi.org/10.1016/0198-0254(87)90136-1

Bishop, J. K. B., & Wood, T. J. (2008). Particulate matter chemistry and dynamics in the twilight zone at VERTIGO ALOHA and K2 sites. *Deep Sea Research Part I: Oceanographic Research Papers*, *55*(12), 1684–1706. https://doi.org/10.1016/j.dsr.2008.07.012

Boeuf, D., Edwards, B. R., Eppley, J. M., Hu, S. K., Poff, K. E., Romano, A. E., et al. (2019). Biological composition and microbial dynamics of sinking particulate organic matter at abyssal depths in the oligotrophic open ocean. *Proceedings of the National Academy of Sciences*, *116*(24), 11824–11832. https://doi.org/10.1073/pnas.1903080116

Boyd, P. W., Claustre, H., Levy, M., Siegel, D. A., & Weber, T. (2019). Multi-faceted particle pumps drive carbon sequestration in the ocean. *Nature*, *568*(7752), 327–335. https://doi.org/10.1038/s41586-019-1098-2

Broecker, W., & Clark, E. (2009). Ratio of coccolith $CaCO_3$ to foraminifera $CaCO_3$ in late Holocene deep sea sediments. *Paleoceanography*, *24*(3), 1–11. https://doi.org/10.1029/2009pa001731

Buitenhuis, E. T., Quéré, C. L., Bednaršek, N., & Schiebel, R. (2019). Large contribution of pteropods to shallow $CaCO_3$ export. *Global Biogeochemical Cycles*, *145*(2), 1–11. https://doi.org/10.1029/2018gb006110

Burd, A. B., & Jackson, G. A. (2009). Particle aggregation. *Annual Review of Marine Science*, *1*(1), 65–90. https://doi.org/10.1146/annurev.marine.010908.163904

Burdige, D. J., Hu, X., & Zimmerman, R. C. (2010). The widespread occurrence of coupled carbonate dissolution/reprecipitation in surface sediments on the Bahamas Bank. *American Journal of Science*, *310*(6), 492–521. https://doi.org/10.2475/06.2010.03

Cael, B. B., Cavan, E. L., & Britten, G. L. (2021). Reconciling the size-dependence of marine particle sinking speed. *Geophysical Research Letters*, *48*(5). https://doi.org/10.1029/2020gl091771

Carter, B. R., Feely, R. A., Lauvset, S. K., Olsen, A., DeVries, T., & Sonnerup, R. (2021). Preformed properties for marine organic matter and carbonate mineral cycling quantification. *Global Biogeochemical Cycles*, *35*(1), e2020GB006623. https://doi.org/10.1029/2020GB006623

Carter, B. R., Toggweiler, J. R., Key, R. M., & Sarmiento, J. L. (2014). Processes determining the marine alkalinity and calcium carbonate saturation state distributions. *Biogeosciences*, *11*(24), 7349–7362. https://doi.org/10.5194/bg-11-7349-2014

Chiu, T., & Broecker, W. S. (2008). Toward better paleocarbonate ion reconstructions: New insights regarding the $CaCO_3$ size index. *Paleoceanography*, *23*(2). https://doi.org/10.1029/2008pa001599

Chung, S.-N., Lee, K., Feely, R. A., Sabine, C. L., Millero, F. J., Wanninkhof, R., et al. (2003). Calcium carbonate budget in the Atlantic Ocean based on water column inorganic carbon chemistry. *Global Biogeochemical Cycles*, *17*(4). https://doi.org/10.1029/2002gb002001

Collins, J. R., Edwards, B. R., Thamatrakoln, K., Ossolinski, J. E., DiTullio, G. R., Bidle, K. D., et al. (2015). The multiple fates of sinking particles in the North Atlantic Ocean. *Global Biogeochemical Cycles*, *29*(9), 1471–1494. https://doi.org/10.1002/2014gb005037

De La Rocha, C., Nowald, N., & Passow, U. (2008). Interactions between diatom aggregates, minerals, particulate organic carbon, and dissolved organic matter: Further implications for the ballast hypothesis. *Global Biogeochemical Cycles*, *22*(4). https://doi.org/10.1029/2007gb003156

Dilling, L., & Alldredge, A. L. (2000). Fragmentation of marine snow by swimming macrozooplankton: A new process impacting carbon cycling in the sea. *Deep Sea Research Part I: Oceanographic Research Papers*, *47*(7), 1227–1245. https://doi.org/10.1016/s0967-0637(99)00105-3

Dong, S., Berelson, W. M., Adkins, J. F., Rollins, N. E., Naviaux, J. D., Pirbadian, S., et al. (2020). An atomic force microscopy study of calcite dissolution in seawater. *Geochimica et Cosmochimica Acta*, *283*, 40–53. https://doi.org/10.1016/j.gca.2020.05.031

Dong, S., Berelson, W. M., Rollins, N. E., Subhas, A. V., Naviaux, J. D., Celestian, A. J., et al. (2019). Aragonite dissolution kinetics and calcite/aragonite ratios in sinking and suspended particles in the North Pacific. *Earth and Planetary Science Letters*, *515*, 1–12. https://doi.org/10.1016/j.epsl.2019.03.016

Dong, S., Berelson, W. M., Teng, H. H., Rollins, N. E., Pirbadian, S., El-Naggar, M. Y., & Adkins, J. F. (2020). A mechanistic study of carbonic anhydrase-enhanced calcite dissolution. *Geophysical Research Letters*, *47*(19). https://doi.org/10.1029/2020gl089244

Dunne, J. P., Hales, B., & Toggweiler, J. R. (2012). Global calcite cycling constrained by sediment preservation controls. *Global Biogeochemical Cycles*, *26*(3). https://doi.org/10.1029/2010gb003935

Durkin, C. A., Estapa, M. L., & Buesseler, K. O. (2015). Observations of carbon export by small sinking particles in the upper mesopelagic. *Marine Chemistry*, *175*(C), 72–81. https://doi.org/10.1016/j.marchem.2015.02.011

Eide, M., Olsen, A., Ninnemann, U. S., & Eldevik, T. (2017). A global estimate of the full oceanic [13]C Suess effect since the preindustrial. *Global Biogeochemical Cycles*, *31*(3), 492–514. https://doi.org/10.1002/2016gb005472

Eide, M., Olsen, A., Ninnemann, U. S., & Johannessen, T. (2017). A global ocean climatology of preindustrial and modern ocean $\delta^{13}C$. *Global Biogeochemical Cycles*, *31*(3), 515–534. https://doi.org/10.1002/2016gb005473

Emerson, S., & Bender, M. (1981). Carbon fluxes at the sediment-water interface of the deep-sea: Calcium carbonate preservation. *Journal of Marine Research*, *39*, 139–162.

Emerson, S. R., & Archer, D. (1990). Calcium carbonate preservation in the ocean. *Philosophical Transactions of the Royal Society of London - Series A: Mathematical and Physical Sciences*, *331*(1616), 29–40.

Endo, H., Ogata, H., & Suzuki, K. (2018). Contrasting biogeography and diversity patterns between diatoms and haptophytes in the central Pacific Ocean. *Scientific Reports*, *8*(1), 10916. https://doi.org/10.1038/s41598-018-29039-9

Feely, R. A., Sabine, C. L., Lee, K., Millero, F. J., Lamb, M. F., Greeley, D., et al. (2002). In situ calcium carbonate dissolution in the Pacific Ocean. *Global Biogeochemical Cycles*, *16*(4), 91-1–91-12. https://doi.org/10.1029/2002gb001866

Fischer, G., & Karakaş, G. (2009). Sinking rates and ballast composition of particles in the Atlantic Ocean: Implications for the organic carbon fluxes to the deep ocean. *Biogeosciences*, *6*(1), 85–102. https://doi.org/10.5194/bg-6-85-2009

Friis, K., Najjar, R. G., Follows, M. J., & Dutkiewicz, S. (2006). Possible overestimation of shallow-depth calcium carbonate dissolution in the ocean. *Global Biogeochemical Cycles*, *20*(4). https://doi.org/10.1029/2006gb002727

Fukuhara, T., Tanaka, Y., Ioka, N., & Nishimura, A. (2008). An in situ experiment of calcium carbonate dissolution in the central Pacific Ocean. *International Journal of Greenhouse Gas Control*, *2*(1), 78–88. https://doi.org/10.1016/s1750-5836(07)00085-0

Gehlen, M., Bassinot, F. C., Chou, L., & McCorkle, D. (2005). Reassessing the dissolution of marine carbonates: II. Reaction kinetics. *Deep Sea Research Part I: Oceanographic Research Papers*, *52*(8), 1461–1476. https://doi.org/10.1016/j.dsr.2005.03.011

Grabowski, E., Letelier, R. M., Laws, E. A., & Karl, D. M. (2019). Coupling carbon and energy fluxes in the North Pacific Subtropical Gyre. *Nature Communications*, *10*(1), 1895. https://doi.org/10.1038/s41467-019-09772-z

Greenwood, J. (2009). Shallow water dissolution of settling calcite at Station ALOHA. *Limnology and Oceanography*, *54*(5), 1420–1424. https://doi.org/10.4319/lo.2009.54.5.1420

Guidi, L., Jackson, G. A., Stemmann, L., Miquel, J. C., Picheral, M., & Gorsky, G. (2008). Relationship between particle size distribution and flux in the mesopelagic zone. *Deep Sea Research Part I: Oceanographic Research Papers*, *55*(10), 1364–1374. https://doi.org/10.1016/j.dsr.2008.05.014

Harris, R. P. (1994). Zooplankton grazing on the coccolithophore Emiliania huxleyi and its role in inorganic carbon flux. *Marine Biology*, *119*(3), 431–439. https://doi.org/10.1007/bf00347540

Haskell, W. Z., Prokopenko, M. G., Hammond, D. E., Stanley, R. H. R., Berelson, W. M., Baronas, J. J., et al. (2016). An organic carbon budget for coastal Southern California determined by estimates of vertical nutrient flux, net community production and export. *Deep Sea Research Part I: Oceanographic Research Papers*, *116*, 49–76. https://doi.org/10.1016/j.dsr.2016.07.003

Henson, S., Moigne, F. L., & Giering, S. (2019). Drivers of carbon export efficiency in the global ocean. *Global Biogeochemical Cycles*, *33*(7), 891–903. https://doi.org/10.1029/2018gb006158

Holzer, M., DeVries, T., & de Lavergne, C. (2021). Diffusion controls the ventilation of a Pacific Shadow Zone above abyssal overturning. *Nature Communications*, *12*(1), 4348. https://doi.org/10.1038/s41467-021-24648-x

Honjo, S. (1976). Coccoliths: Production, transportation and sedimentation. *Marine Micropaleontology*, *1*, 65–79. https://doi.org/10.1016/0377-8398(76)90005-0

Honjo, S., & Erez, J. (1978). Dissolution rates of calcium carbonate in the deep ocean; an in situ experiment in the North Atlantic Ocean. *Earth and Planetary Science Letters*, *40*(2), 287–300. https://doi.org/10.1016/0012-821x(78)90099-7

Hou, Y., Hammond, D. E., Berelson, W. M., Kemnitz, N., Adkins, J. F., & Lunstrum, A. (2019). Spatial patterns of benthic silica flux in the North Pacific reflect upper ocean production. *Deep Sea Research Part I: Oceanographic Research Papers*, *148*, 25–33. https://doi.org/10.1016/j.dsr.2019.04.013

Iversen, M. H., & Ploug, H. (2010). Ballast minerals and the sinking carbon flux in the ocean: Carbon-specific respiration rates and sinking velocity of marine snow aggregates. *Biogeosciences*, *7*(9), 2613–2624. https://doi.org/10.5194/bg-7-2613-2010

Iversen, M. H., & Poulsen, L. (2007). Coprorhexy, coprophagy, and coprochaly in the copepods Calanus helgolandicus, Pseudocalanus elongatus, and Oithona similis. *Marine Ecology Progress Series*, *350*, 79–89. https://doi.org/10.3354/meps07095

Jansen, H., & Wolf-Gladrow, D. A. (2001). Carbonate dissolution in copepod guts: A numerical model. *Marine Ecology Progress Series*, *221*, 199–207. https://doi.org/10.3354/meps221199

Jansen, H., Zeebe, R. E., & Wolf-Gladrow, D. A. (2002). Modeling the dissolution of settling $CaCO_3$ in the ocean. *Global Biogeochemical Cycles*, *16*(2), 11-1–11-16. https://doi.org/10.1029/2000gb001279

Jeansson, E., Steinfeldt, R., & Tanhua, T. (2021). *Water mass ages based on GLODAPv2 data product* (NCEI Accession 0226793). NOAA National Centers for Environmental Information. https://doi.org/10.25921/xp33-q351

Juranek, L. W., Quay, P. D., Feely, R. A., Lockwood, D., Karl, D. M., & Church, M. J. (2012). Biological production in the NE Pacific and its influence on air-sea CO_2 flux: Evidence from dissolved oxygen isotopes and O_2/Ar. *Journal of Geophysical Research*, *117*(C5). https://doi.org/10.1029/2011jc007450

Kawahata, H., Nishimura, A., & Gagan, M. K. (2002). Seasonal change in foraminiferal production in the western equatorial Pacific warm pool: Evidence from sediment trap experiments. *Deep Sea Research Part II: Topical Studies in Oceanography*, *49*(13–14), 2783–2800. https://doi.org/10.1016/s0967-0645(02)00058-9

Keir, R. S. (1980). The dissolution kinetics of biogenic calcium carbonates in seawater. *Geochimica et Cosmochimica Acta*, *44*(2), 241–252. https://doi.org/10.1016/0016-7037(80)90135-0

Klaas, C., & Archer, D. E. (2002). Association of sinking organic matter with various types of mineral ballast in the deep sea: Implications for the rain ratio. *Global Biogeochemical Cycles*, *16*(4), 63-1–63-14. https://doi.org/10.1029/2001gb001765

Laber, C. P., Hunter, J. E., Carvalho, F., Collins, J. R., Hunter, E. J., Schieler, B. M., et al. (2018). Coccolithovirus facilitation of carbon export in the North Atlantic. *Nature Microbiology*, *3*(5), 537–547. https://doi.org/10.1038/s41564-018-0128-4

Lam, P. J., Lee, J.-M., Heller, M. I., Mehic, S., Xiang, Y., & Bates, N. R. (2018). Size-fractionated distributions of suspended particle concentration and major phase composition from the U.S. GEOTRACES Eastern Pacific Zonal Transect (GP16). *Marine Chemistry*, *201*, 90–107. https://doi.org/10.1016/j.marchem.2017.08.013i

Lam, P. J., & Marchal, O. (2015). Insights into particle cycling from thorium and particle data. *Annual Review of Marine Science*, *7*(1), 1–26. https://doi.org/10.1146/annurev-marine-010814-015623

Marsay, C. M., Sanders, R. J., Henson, S. A., Pabortsava, K., Achterberg, E. P., & Lampitt, R. S. (2015). Attenuation of sinking particulate organic carbon flux through the mesopelagic ocean. *Proceedings of the National Academy of Sciences*, *112*(4), 1089–1094. https://doi.org/10.1073/pnas.1415311112

Martin, J. H., Knauer, G. A., Karl, D. M., & Broenkow, W. W. (1987). VERTEX: Carbon cycling in the northeast Pacific. *Deep Sea Research*, *34*(2), 267–285. https://doi.org/10.1016/0198-0149(87)90086-0

McCorkle, D. C., & Emerson, S. R. (1988). The relationship between pore water carbon isotopic composition and bottom water oxygen concentration. *Geochimica et Cosmochimica Acta*, *52*(5), 1169–1178. https://doi.org/10.1016/0016-7037(88)90270-0

McDonnell, A. M. P., & Buesseler, K. O. (2010). Variability in the average sinking velocity of marine particles. *Limnology and Oceanography*, *55*(5), 2085–2096. https://doi.org/10.4319/lo.2010.55.5.2085

Milliman, J. D., Troy, P. J., Balch, W. M., Adams, A. K., Li, Y. H., & Mackenzie, F. (1999). Biologically mediated dissolution of calcium carbonate above the chemical lysocline? *Deep Sea Research*, *46*(10), 1653–1669. https://doi.org/10.1016/s0967-0637(99)00034-5

Naviaux, J. D., Subhas, A. V., Dong, S., Rollins, N. E., Liu, X., Byrne, R. H., et al. (2019). Calcite dissolution rates in seawater: Lab vs. in situ measurements and inhibition by organic matter. *Marine Chemistry*, *215*, 103684. https://doi.org/10.1016/j.marchem.2019.103684

Naviaux, J. D., Subhas, A. V., Rollins, N. E., Dong, S., Berelson, W. M., & Adkins, J. F. (2019). Temperature dependence of calcite dissolution kinetics in seawater. *Geochimica et Cosmochimica Acta*, *246*, 363–384. https://doi.org/10.1016/j.gca.2018.11.037

Oakes, R. L., Peck, V. L., Manno, C., & Bralower, T. J. (2019). Impact of preservation techniques on pteropod shell condition. *Polar Biology*, *42*(2), 257–269. https://doi.org/10.1007/s00300-018-2419-x

Olsen, A., Lange, N., Key, R. M., Tanhua, T., Alvarez, M., Becker, S., et al. (2019). GLODAPv2. 2019–an update of GLODAPv2. *Earth System Science Data Discussions*. https://doi.org/10.5194/essd-2019-66

Omand, M. M., Govindarajan, R., He, J., & Mahadevan, A. (2020). Sinking flux of particulate organic matter in the oceans: Sensitivity to particle characteristics. *Scientific Reports*, *10*(1), 5582. https://doi.org/10.1038/s41598-020-60424-5

Passow, U., & De La Rocha, C. L. (2006). Accumulation of mineral ballast on organic aggregates. *Global Biogeochemical Cycles*, *20*(1). https://doi.org/10.1029/2005gb002579

Pataki, D. E., Ehleringer, J. R., Flanagan, L. B., Yakir, D., Bowling, D. R., Still, C. J., et al. (2003). The application and interpretation of Keeling plots in terrestrial carbon cycle research. *Global Biogeochemical Cycles*, *17*(1). https://doi.org/10.1029/2001gb001850

Peck, V. L., Oakes, R. L., Harper, E. M., Manno, C., & Tarling, G. A. (2018). Pteropods counter mechanical damage and dissolution through extensive shell repair. *Nature Communications*, *9*, 1–7. https://doi.org/10.1038/s41467-017-02692-w

Peterson, M. N. (1966). Calcite: Rates of dissolution in a vertical profile in central Pacific. *Science*, *154*(3756), 1542–1544. https://doi.org/10.1126/science.154.3756.1542

Ploug, H. (2001). Small-scale oxygen fluxes and remineralization in sinking aggregates. *Limnology and Oceanography*, *46*(7), 1624–1631. https://doi.org/10.4319/lo.2001.46.7.1624

Ploug, H., Iversen, M. H., & Fischer, G. (2008). Ballast, sinking velocity, and apparent diffusivity within marine snow and zooplankton fecal pellets: Implications for substrate turnover by attached bacteria. *Limnology and Oceanography*, *53*(5), 1878–1886. https://doi.org/10.4319/lo.2008.53.5.1878

Ploug, H., Kühl, M., Buchholz-Cleven, B., & Jørgensen, B. (1997). Anoxic aggregates—An ephemeral phenomenon in the pelagic environment? *Aquatic Microbial Ecology*, *13*, 285–294. https://doi.org/10.3354/ame013285

Pond, D. W., Harris, R. P., & Brownlee, C. (1995). A microinjection technique using a pH-sensitive dye to determine the gut pH of Calanus helgolandicus. *Marine Biology*, *123*(1), 75–79. https://doi.org/10.1007/bf00350325

Riley, J. S., Sanders, R., Marsay, C., Moigne, F. A. C. L., Achterberg, E. P., & Poulton, A. J. (2012). The relative contribution of fast and slow sinking particles to ocean carbon export. *Global Biogeochemical Cycles*, *26*(1). https://doi.org/10.1029/2011gb004085

Rosas-Navarro, A., Langer, G., & Ziveri, P. (2018). Temperature effects on sinking velocity of different *Emiliania huxleyi* strains. *PLoS One*, *13*(3), e0194386. https://doi.org/10.1371/journal.pone.0194386

Sabine, C. L., Feely, R. A., Gruber, N., Key, R. M., Lee, K., Bullister, J. L., et al. (2004). The oceanic sink for anthropogenic CO_2. *Science*, *305*(5682), 367–371. https://doi.org/10.1126/science.1097403

Smith, K. L., Jr., Ruhl, H. A., Huffard, C. L., Messié, M., & Kahru, M. (2018). Episodic organic carbon fluxes from surface ocean to abyssal depths during long-term monitoring in NE Pacific. *Proceedings of the National Academy of Sciences*, *115*(48), 12235–12240. https://doi.org/10.1073/pnas.1814559115

Steinberg, D. K., & Landry, M. R. (2014). Zooplankton and the ocean carbon cycle. *Annual Review of Marine Science*, *9*(1), 413–444. https://doi.org/10.1146/annurev-marine-010814-015924

Steinberg, D. K., Mooy, B. A. S. V., Buesseler, K. O., Boyd, P. W., Kobari, T., & Karl, D. M. (2008). Bacterial vs. zooplankton control of sinking particle flux in the ocean's twilight zone. *Limnology and Oceanography*, *53*(4), 1327–1338. https://doi.org/10.4319/lo.2008.53.4.1327

Steiner, Z., Lazar, B., Reimers, C. E., & Erez, J. (2019). Carbonates dissolution and precipitation in hemipelagic sediments overlaid by supersaturated bottom-waters – Gulf of Aqaba, Red Sea. *Geochimica et Cosmochimica Acta*, *246*, 565–580. https://doi.org/10.1016/j.gca.2018.12.007

Stemmann, L., Jackson, G. A., & Ianson, D. (2004). A vertical model of particle size distributions and fluxes in the midwater column that includes biological and physical processes—Part I: Model formulation. *Deep Sea Research Part I: Oceanographic Research Papers*, *51*(7), 865–884. https://doi.org/10.1016/j.dsr.2004.03.001

Stukel, M. R., Ohman, M. D., Kelly, T. B., & Biard, T. (2019). The roles of suspension-feeding and flux-feeding zooplankton as gatekeepers of particle flux into the mesopelagic ocean in the northeast Pacific. *Frontiers in Marine Science*, *6*, 397. https://doi.org/10.3389/fmars.2019.00397

Subhas, A. V., Adkins, J. F., Dong, S., Rollins, N. E., & Berelson, W. M. (2019). The carbonic anhydrase activity of sinking and suspended particles in the North Pacific Ocean. *Limnology and Oceanography*, *65*(3), 637–651. https://doi.org/10.1002/lno.11332

Subhas, A. V., Adkins, J. F., Rollins, N. E., Naviaux, J., Erez, J., & Berelson, W. M. (2017). Catalysis and chemical mechanisms of calcite dissolution in seawater. *Proceedings of the National Academy of Sciences*, *114*(31), 8175–8180. https://doi.org/10.1073/pnas.1703604114

Subhas, A. V., McCorkle, D. C., Quizon, A., McNichol, A. P., & Long, M. H. (2019). Selective preservation of coccolith calcite in Ontong-Java Plateau sediments. *Paleoceanography and Paleoclimatology*, *34*(12), 2141–2157. https://doi.org/10.1029/2019pa003731

Subhas, A. V., Rollins, N. E., Berelson, W. M., Dong, S., Erez, J., & Adkins, J. F. (2015). A novel determination of calcite dissolution kinetics in seawater. *Geochimica et Cosmochimica Acta*, *170*(C), 51–68. https://doi.org/10.1016/j.gca.2015.08.011

Subhas, A. V., Rollins, N. E., Berelson, W. M., Erez, J., Ziveri, P., Langer, G., & Adkins, J. F. (2018). The dissolution behavior of biogenic calcites in seawater and a possible role for magnesium and organic carbon. *Marine Chemistry*, *205*, 100–112. https://doi.org/10.1016/j.marchem.2018.08.001

Sulpis, O., Jeansson, E., Dinauer, A., Lauvset, S. K., & Middelburg, J. J. (2021). Calcium carbonate dissolution patterns in the ocean. *Nature Geoscience*, *14*, 1–6. https://doi.org/10.1038/s41561-021-00743-y

Talley, L. D. (1993). Distribution and formation of North Pacific intermediate water. *Journal of Physical Oceanography*, *23*(3), 517–537. https://doi.org/10.1175/1520-0485(1993)023<0517:dafonp>2.0.co;2

Timothy, D. A., Wong, C. S., Barwell-Clarke, J. E., Page, J. S., White, L. A., & Macdonald, R. W. (2013). Climatology of sediment flux and composition in the subarctic Northeast Pacific Ocean with biogeochemical implications. *Progress in Oceanography*, *116*, 95–129. https://doi.org/10.1016/j.pocean.2013.06.017

Troy, P. J., Li, Y. H., & Mackenzie, F. T. (1997). Changes in surface morphology of calcite exposed to the oceanic water column. *Aquatic Geochemistry*, *3*, 1–20. https://doi.org/10.1023/A:1009652821575

Turner, J. T. (2015). Zooplankton fecal pellets, marine snow, phytodetritus and the ocean's biological pump. *Progress in Oceanography*, *130*, 205–248. https://doi.org/10.1016/j.pocean.2014.08.005

Walker, J. M., & Langer, G. (2021). Coccolith crystals: Pure calcite or organic-mineral composite structures? *Acta Biomaterialia*, *125*, 83–89. https://doi.org/10.1016/j.actbio.2021.02.025

Waugh, D. W., Hall, T. M., & Haine, T. W. N. (2003). Relationships among tracer ages. *Journal of Geophysical Research* (C5), 108. https://doi.org/10.1029/2002jc001325

White, M. M., Waller, J. D., Lubelczyk, L. C., Drapeau, D. T., Bowler, B. C., Balch, W. M., & Fields, D. M. (2018). Coccolith dissolution within copepod guts affects fecal pellet density and sinking rate. *Scientific Reports*, *8*(1), 9758. https://doi.org/10.1038/s41598-018-28073-x

Wilson, R. W., Millero, F. J., Taylor, J. R., Walsh, P. J., Christensen, V., Jennings, S., & Grosell, M. (2009). Contribution of fish to the marine inorganic carbon cycle. *Science*, *323*(5912), 359–362. https://doi.org/10.1016/j.pepi.2008.05.007

Wilson, S. E., Steinberg, D. K., & Buesseler, K. O. (2008). Changes in fecal pellet characteristics with depth as indicators of zooplankton repackaging of particles in the mesopelagic zone of the subtropical and subarctic North Pacific Ocean. *Deep Sea Research Part II: Topical Studies in Oceanography*, *55*(14–15), 1636–1647. https://doi.org/10.1016/j.dsr2.2008.04.019

Wong, C. S., Whitney, F. A., Crawford, D. W., Iseki, K., Matear, R. J., Johnson, W. K., et al. (1999). Seasonal and interannual variability in particle fluxes of carbon, nitrogen and silicon from time series of sediment traps at Ocean Station P, 1982–1993: Relationship to changes in subarctic primary productivity. *Deep Sea Research Part II: Topical Studies in Oceanography*, *46*(11–12), 2735–2760. https://doi.org/10.1016/s0967-0645(99)00082-x

Woosley, R. J., Millero, F. J., & Grosell, M. (2012). The solubility of fish-produced high magnesium calcite in seawater. *Journal of Geophysical Research*, *117*(C4). https://doi.org/10.1029/2011jc007599

Zhang, H., Stoll, H., Bolton, C., Jin, X., & Liu, C. (2018). Technical note: A refinement of coccolith separation methods: Measuring the sinking characteristics of coccoliths. *Biogeosciences*, *15*(15), 4759–4775. https://doi.org/10.5194/bg-15-4759-2018

Ziveri, P., Broerse, A., van Hinte, J. E., Westbroek, P., & Honjo, S. (2000). The fate of coccoliths at 48°N 21°W, northeastern Atlantic. *Deep Sea Research*, *47*(9–11), 1853–1875. https://doi.org/10.1016/s0967-0645(00)00009-6

Ziveri, P., Gray, W., Ortiz, G., Manno, C., Grelaud, M., Incarbona, A., et al. (2022). Pelagic carbonate production in the North Pacific Ocean. In *Revision at Nature Communications*.

References From the Supporting Information

Carter, B. R., Feely, R. A., Williams, N. L., Dickson, A. G., Fong, M. B., & Takeshita, Y. (2017). Updated methods for global locally interpolated estimation of alkalinity, pH, and nitrate. *Limnology and Oceanography: Methods*, *16*(2), 119–131. https://doi.org/10.1002/lom3.10232

de Lavergne, C., Vic, C., Madec, G., Roquet, F., Waterhouse, A. F., Whalen, C. B., et al. (2020). A parameterization of local and remote tidal mixing. *Journal of Advances in Modeling Earth Systems*, *12*(5). https://doi.org/10.1029/2020ms002065

Graven, H., Allison, C. E., Etheridge, D. M., Hammer, S., Keeling, R. F., Levin, I., et al. (2017). Compiled records of carbon isotopes in atmospheric CO_2 for historical simulations in CMIP6. *Geoscientific Model Development*, *10*(12), 4405–4417. https://doi.org/10.5194/gmd-10-4405-2017

Haskell, W. Z., Kadko, D., Hammond, D. E., Knapp, A. N., Prokopenko, M. G., Berelson, W. M., & Capone, D. G. (2015). Upwelling velocity and eddy diffusivity from [7]Be measurements used to compare vertical nutrient flux to export POC flux in the Eastern Tropical South Pacific. *Marine Chemistry*, *168*, 140–150. https://doi.org/10.1016/j.marchem.2014.10.004

Körtzinger, A., Quay, P. D., & Sonnerup, R. E. (2003). Relationship between anthropogenic CO_2 and the ^{13}C suess effect in the North Atlantic Ocean. *Global Biogeochemical Cycles*, *17*(1), 5-1–5-20. https://doi.org/10.1029/2001gb001427

Olsen, A., & Ninnemann, U. (2010). Large $\delta^{13}C$ gradients in the preindustrial North Atlantic revealed. *Science*, *330*(6004), 658–659. https://doi.org/10.1126/science.1193769

Warner, M. J., & Weiss, R. F. (1985). Solubilities of chlorofluorocarbons 11 and 12 in water and seawater. *Deep Sea Research Part A. Oceanographic Research Papers*, *32*(12), 1485–1497. https://doi.org/10.1016/0198-0149(85)90099-8

Watson, A. J., & Ledwell, J. R. (2000). Oceanographic tracer release experiments using sulphur hexafluoride. *Journal of Geophysical Research*, *105*(C6), 14325–14337. https://doi.org/10.1029/1999jc900272